

1218 NACA TN No. 1634 8121

0144520



# NATIONAL ADVISORY COMMITTEE FOR AERONAUTICS

## TECHNICAL NOTE

No. 1634

### WIND-TUNNEL TESTS AND ANALYSIS OF TWO 10-FOOT-DIAMETER SIX-BLADE DUAL-ROTATING TRACTOR PROPELLERS DIFFERING IN PITCH DISTRIBUTION

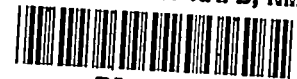
By Jean Gilman, Jr.

Langley Memorial Aeronautical Laboratory  
Langley Field, Va.



Washington  
June 1948

AFMDC  
TECHNICAL LIBRARY  
1948



## TECHNICAL NOTE NO. 1634

WIND-TUNNEL TESTS AND ANALYSIS OF TWO 10-FOOT-DIAMETER  
SIX-BLADE DUAL-ROTATING TRACTOR PROPELLERS  
DIFFERING IN PITCH DISTRIBUTION

By Jean Gilman, Jr.

## SUMMARY

An investigation was conducted at the Langley propeller-research tunnel to determine the efficiency at low tip speeds of two 10-foot-diameter six-blade dual-rotating propellers differing only in pitch distribution. Propeller forces were determined from wind-tunnel tests and were also calculated by an analytical method by use of two-dimensional airfoil section data. Wake surveys were made in order to compare the measured thrust loadings with the calculated thrust loadings.

Comparisons were made between the experimental and analytically derived efficiency, blade loading, thrust, and torque characteristics of the two propellers for a wide range of operating conditions. The analysis included the determination of the energy losses due to induced flow and to profile drag for several representative operating conditions.

Satisfactory agreement was obtained between test data and calculated data. A dual-rotating propeller of low design pitch maintained high efficiency at advance ratios greater than 2.5 as contrasted with the serious losses resulting from operation of a similar single-rotating propeller in the same range. The induced efficiency of dual-rotating propellers near peak efficiency was relatively independent of blade load distribution.

## INTRODUCTION

Experimental results (references 1 to 3) have established the fact that at advance ratios in excess of approximately 2.5, and at correspondingly high power coefficients, the dual-rotating propeller is more efficient than a geometrically similar single-rotating propeller with the same number of blades. Theoretical researches have not as yet provided an optimum design method for dual-rotating propellers as Betz and other investigators have formulated for single-rotating propellers, but means have been provided (for example, reference 4) for analytically determining the characteristics of dual-rotating propellers from basic two-dimensional airfoil section data.

In addition to the lack of a well-established design procedure for dual-rotating propellers, information is scarce as to the effects of blade load

distribution on efficiency. The purpose of this investigation was to determine these effects by analyzing the performance of two 6-blade dual-rotating propellers differing only in pitch distribution. The present investigation is a continuation of a similar analysis of three 3-blade single-rotating propellers discussed in reference 5.

Experimental force-balance data were obtained from tests of the two 10-foot-diameter propellers at low tip speeds over a blade-angle range of  $15^\circ$  to  $65^\circ$ , and wake surveys were made to determine the radial thrust distribution near peak efficiency. Comparisons were made also between the experimental results and analytically derived torque, thrust, blade loading, and efficiency characteristics of the two propellers for a wide range of operating conditions. The energy losses of the two propellers were analyzed for three representative flight conditions and finally some general design considerations were discussed.

#### SYMBOLS AND COEFFICIENTS

$a$	axial inflow factor
$\bar{a}$	axial inflow factor of one component including the effect of the other component
$a'$	rotational inflow factor
$\bar{a}'$	rotational inflow factor of one component including the effect of the other component
$b$	blade section chord, feet
$c_d$	section profile-drag coefficient $(dD/qb)$
$c_l$	section lift coefficient $(dL/qb)$
$c_{l_d}$	design section lift coefficient
$C_P$	power coefficient $(P/\rho n^3 D^5 \text{ or } 2\pi C_Q)$
$C_Q$	torque coefficient $(Q/\rho n^2 D^5)$
$C_T$	thrust coefficient $(T_p/\rho n^2 D^4)$
$D$	propeller diameter, feet; drag, pounds
$\Delta D$	change in body drag due to propeller slipstream, pounds
$dC_Q/dx$	section torque coefficient $\left( \frac{dQ/dx}{\rho n^2 D^5} \right)$

$dC_T/dx$	section thrust coefficient $\left(\frac{dT/dx}{\rho n^2 D^4}\right)$
$dQ/r$	section torque force, pounds
$dT$	section thrust force, pounds
$E_a$	energy lost to axial momentum in propeller wake, foot-pounds per second
$E_D$	energy lost through profile drag, foot-pounds per second
$E_r$	energy lost to rotational momentum in propeller wake, foot-pounds per second
$G$	Goldstein induced-velocity correction factor for finite number of blades ( $F$ in notation of references 4 and 5)
$\Delta H$	total-pressure rise in propeller wake, pounds per square foot
$h$	maximum thickness of blade section, feet
$J$	advance ratio ( $V/nD$ )
$L$	lift, pounds
$n$	propeller rotational speed, revolutions per second
$P$	power absorbed by propeller, foot-pounds per second ( $2\pi nQ$ )
$Q$	torque of propeller, pounds-foot
$q$	dynamic pressure, pounds per square foot
$R$	radius to propeller tip, feet
$r$	radius to propeller section, feet
$T$	shaft tension, pounds
$T_p$	propulsive thrust, pounds ( $T - \Delta D$ )
$V$	free-stream velocity, feet per second
$V_z$	local axial velocity, propeller removed, feet per second
$x$	radius ratio ( $r/R$ )
$x_0$	radius ratio at spinner juncture

$\beta$  blade-section angle, degrees

$$\gamma = \tan^{-1} c_d/c_l$$

$\eta$  propulsive efficiency ( $T_p V/P$  or  $C_T J/C_P$ )

$\eta'_0$  blade-section profile-drag efficiency

$\rho$  mass density of air, slugs per cubic foot

$\rho_0$  standard sea-level mass density, slugs per cubic foot

$\phi$  aerodynamic helix angle, degrees (fig. 1)

$\phi_0$  geometric helix angle, degrees  $\left(\tan^{-1} \frac{J}{\pi x}, \text{fig. 1}\right)$

Subscripts:

F front component

R rear component

i ideal actuator disk

opt Betz optimum loading for single-rotating propellers

#### EQUATIONS AND METHODS OF ANALYSIS

The method of analysis employed in reference 5 to determine blade-load-distribution effects on efficiency was used in the investigation presented herein. As in reference 5, the total-pressure rise in the propeller wake was converted into terms of section thrust by the equation

$$\frac{dC_T}{dx} = \frac{\Delta H}{q} \frac{\pi}{4} J^2 x \quad (1)$$

Section thrust and torque coefficients were calculated from two-dimensional airfoil section data by the method given in reference 4. The airfoil section data (fig. 2) were interpolated from reference 6.

The calculations of dual-rotating-propeller characteristics are based on the mutual interaction of the front and rear components. (See fig. 1.) The equations of reference 5 for determining the induced energy losses require some modification to account for this interaction. The axial energy loss is

$$dE_a = aV dT$$

where

$$aV = (\bar{a}_F + \bar{a}_R)V$$

and

$$dT = dT_F + dT_R$$

or

$$dE_a = V(\bar{a}_F + \bar{a}_R)(dT_F + dT_R)$$

In nondimensional form this equation becomes

$$\frac{E_a}{P} = \frac{J}{C_P} \int_{x_0}^{1.0} (\bar{a}_F + \bar{a}_R) \left[ \left( \frac{dC_T}{dx} \right)_F + \left( \frac{dC_T}{dx} \right)_R \right] dx \quad (2)$$

The quantity  $\bar{a}$  is determined from the relation

$$\bar{a}_F \text{ or } R = \frac{-1 + \sqrt{1 + \frac{4 \left( \frac{dC_T}{dx} \right)_F \text{ or } R}{\pi J^2 x(G)_F \text{ or } R}}}{2}$$

The rotational energy loss is

$$dE_r = a' 2\pi n \frac{dQ}{r}$$

Since  $n_F$  and  $n_R$  are opposite, then

$$a' 2\pi n = (\bar{a}'_F - \bar{a}'_R) 2\pi n$$

and, for the same reason, the net torque force with respect to the wake is

$$\frac{dQ}{r} = \left( \frac{dQ}{r} \right)_F - \left( \frac{dQ}{r} \right)_R$$

The rotational energy loss, therefore, is

$$dE_r = 2\pi n (\bar{a}'_F - \bar{a}'_R) (dQ_F - dQ_R)$$

In nondimensional form this equation becomes

$$\frac{E_r}{P} = \frac{1}{C_Q} \int_{x_0}^{1.0} (\bar{a}'_F - \bar{a}'_R) \left[ \left( \frac{dC_Q}{dx} \right)_F - \left( \frac{dC_Q}{dx} \right)_R \right] dx \quad (3)$$

The quantity  $\bar{a}'$  is evaluated from

$$\bar{a}'_F \text{ or } R = \left( \frac{dC_Q}{dx} \right)_F \text{ or } R \frac{2}{\pi^2 J x^3 [(1 + \bar{a})G]_F \text{ or } R}$$

The fractional energy loss due to profile drag is

$$\frac{E_D}{P} = \frac{\left( \frac{E_D}{P} \right)_F C_{P_F} + \left( \frac{E_D}{P} \right)_R C_{P_R}}{C_P} \quad (4)$$

where

$$\left( \frac{E_D}{P} \right)_F \text{ or } R = \frac{1}{C_{Q_F} \text{ or } R} \int_{x_0}^{1.0} \left[ (1 - \eta'_o) \frac{dC_Q}{dx} \right]_F \text{ or } R dx$$

As in reference 5, the value of  $\eta'_o$  can be shown to be

$$(\eta'_o)_F \text{ or } R = \left[ \frac{\tan \phi}{\tan (\phi + \gamma)} \right]_F \text{ or } R \quad (5)$$

Values of  $\phi$  and  $\gamma$ , used in equation (5), were obtained from the original calculations of  $\left( \frac{dC_T}{dx} \right)_F \text{ or } R$  by a method of cross-plotting.

The value of  $x_0$  for this investigation is 0.193 for the front component and 0.236 for the rear component. When the total front and rear contribution is considered, the average value of  $x_0$  is taken to be 0.210.

## APPARATUS

## Propellers

The propellers tested were the NACA 10-(3)(08)-03-30 and the NACA 10-(3)(08)-03-55 and are hereinafter referred to as propellers 30D and 55D, respectively. The numbers 30 and 55 denote the blade-angle setting at 0.75R giving approximately uniform geometric pitch. The blade plan form and thickness distribution are shown in figure 3. A curve showing the variation of the design lift coefficients along the blade is also included in this figure. The activity factor for each blade is 90, and the total activity factor for the 10-foot-diameter six-blade propellers is therefore 540.

An effort was made to attain equal torque along the front and rear blades at peak efficiency for the design front blade-angle settings by having less blade twist in the rear components than in the front components. Thus, the correct difference in  $\beta_{F0.75}$  and  $\beta_{R0.75}$  should result in the maximum cancellation of rotational energy losses. The blades could not feasibly be held to design requirements, however, because they were constructed of mahogany and were very thin for this type of material. The blade-section angles of propeller 55D were generally within  $\pm 0.25^\circ$  of the specified angles, but two of the blades of the rear component of propeller 30D were found to vary as much as  $2^\circ$  from the specified blade-angle distribution over the outer radii.

When the propellers were tested, the blades in each set of three were set at the same angle at the three-quarter radius. An average blade-angle distribution for each component was used in the strip calculations. This average blade-angle distribution for each component is shown in figure 4.

## Test Equipment

The test equipment of reference 5, modified to permit dual rotation, was used for this investigation. The dimensional details of the test setup are given in figure 5.

Each propeller was driven by a 25-horsepower variable-speed electric induction motor which incorporated spring-selsyn dynamometer equipment for measuring torque and an electric tachometer for determining the rotational speed. The propulsive thrust was measured by the regular tunnel thrust-balance equipment.

The pressure rake was mounted horizontally along one radius  $7\frac{1}{2}$  inches (0.0625D) behind the radial center line of the rear component.



The minimum clearance between the blade trailing edge of the rear component and the total-pressure tube at 0.30R was 1.62 inches (0.0135D). The radial center line of the front component was 13 inches forward of that of the rear component. Wake pressures were recorded photographically from an NACA recording multiple-tube manometer. Measurements were taken at the following fractional radii:  $x = 0.30, 0.34, 0.37, 0.42, 0.45, 0.51, 0.55, 0.605, 0.65, 0.75, 0.80, 0.85, 0.90, 0.95, 0.99, 1.03, \text{ and } 1.10$ .

### Tests

Measurements of the propeller forces were made over a range of advance ratios from zero thrust to well beyond the stall for the front blade angles given in the following table:

Propeller	Front blade angle at 0.75 R (deg)									
	15	25	30	35	40	45	50	55	60	65
55D	15	25	30	35	40	45	50	55	60	65
30D	15	25	30	35	--	45	--	55	--	65

The rear blade was set at a slightly lower angle in each case in order to absorb equal power at peak efficiency. The blade-angle differences are shown in figure 6. Equal front and rear rotational speeds were maintained throughout the tests.

The propeller rotational speed was maintained as high as possible (max. attainable, 550 rpm) for the power available (50 hp) while the tunnel speed was increased by steps to obtain the advance ratio for peak efficiency. After reaching peak efficiency, the wind velocity was held constant and the propeller rotational speed was gradually reduced until the value of  $J$  for zero thrust was obtained. The limiting wind velocity was about 90 miles per hour. The Reynolds number, based on the chord at 0.75R and the resultant wind velocity, was approximately  $1 \times 10^6$ . The tip Mach number was always less than 0.3.

The total pressure in the propeller wake was measured over a range of values of  $J$  to include the region of peak efficiency at each blade angle. The results of a velocity survey (propeller removed)  $7\frac{1}{2}$  inches behind the disk of the rear component are presented in figure 7.

At  $\beta_F = 55^\circ$  the deflection of the rear blades varied from about  $0.52^\circ$  at a low value of  $J$  to about  $0.38^\circ$  at peak efficiency. The limited test program did not permit a more extensive check on the blade-angle deflection of the thin wooden blades.

## RESULTS AND DISCUSSION

The results of this investigation are arranged to show: First, the measured propeller operating characteristics; and, second, comparisons between the calculated and measured thrust, torque, efficiency, and blade loading characteristics. Then follow an analysis of the energy losses for the two propellers and a discussion of some design considerations.

It is emphasized here that compressibility effects are not directly considered in the present discussion. The test speeds were far too low to encounter such phenomena; however, the data presented might be considerably altered by compressibility effects under actual flight conditions.

### Propeller Characteristics

Force-balance measurements.— The propeller characteristics determined from the force-balance measurements are given in figures 8 to 11. The propeller operation charts (figs. 8 and 10) show the power-coefficient variation at fixed blade angles and include constant efficiency contours. Figures 9 and 11 give the thrust-coefficient variation.

Wake surveys.— The results of the wake surveys are given in figure 12 for propeller 55D. The data shown were cross-plotted from the original data in order to give the results at standard radii for which curves of the Goldstein factor are readily available. Integrations of thrust-gradient curves constructed from these data yield thrust-coefficient values within 2 or 3 percent of the force-balance values determined.

Comparison of calculated and experimental results.— Figures 8 to 11 include calculated power- and thrust-coefficient curves at blade-angle settings of  $30^\circ$ ,  $45^\circ$ , and  $55^\circ$  for comparison with the measured values. The calculations take into account the velocity gradient due to the spinner (fig. 7). The measured and calculated results for propeller 30D are seen to be in good agreement. The calculated curves for propeller 55D, although generally parallel to the measured values, are shifted to the left. This shift to the left has the appearance of a discrepancy in the blade-angle settings.

A comparison between the measured and calculated blade-element thrust variation with  $J$  at fixed blade-angle settings is given in figure 12 for propeller 55D. The results for propeller 30D are similar. If the discrepancy between the blades which necessitated the use of average blade-angle distributions for making the calculations is considered and also if the very low pressure rises in the wake encountered in these low-speed tests are taken into account, the agreement between data from wake surveys and calculations appears reasonably good.

Figure 13 gives a comparison between an experimental and calculated thrust-gradient curve for propeller 55D at  $\beta_F = 55^\circ$  and  $C_p = 0.65$ .

This comparison at equal values of  $C_p$  and  $\beta_F$  results in a small difference in the values of  $J$  because of the previously mentioned shift to the left of the calculated curves for  $C_T$  as compared with the measured curves for  $C_T$  (fig. 9). The calculated thrust-gradient curve agrees with the measured one closely enough to permit the use of the calculations in analyzing the propeller loadings.

Figure 13 includes a thrust-gradient curve obtained from calculations based on a uniform velocity field (no body interference) for the same blade-angle setting and power coefficient. The comparison between this curve and the other curves shows that the effect of the increased velocity due to the spinner is to reduce the shank loadings.

Figure 14 gives a comparison of peak efficiency envelopes obtained from the measured and calculated results for both propellers. The envelopes from calculations including the body-interference effect are seen to be in agreement with the measured envelopes within experimental accuracy except for propeller 55D at values of  $J$  less than 2.0. The reason for the drop of the measured efficiency envelope of this propeller at the lower values of  $J$  is not understood. The calculations reveal no reason for such a drop.

Figure 14 includes peak efficiency envelopes obtained from calculations with and without body interference. The comparison of these curves shows that even a comparatively small velocity gradient can appreciably affect the peak efficiency.

Comparison of experimental propeller efficiencies.— The efficiency contour curves from experimental data in figure 8 show that propeller 55D has an efficiency of 89 percent or greater for a range of  $J$  from 2.2 to about 4.7. This range of  $J$  for propeller 30D (fig. 10) is from 1.05 to about 3.6. Thus, propeller 55D has an advantage if operation is required at advance ratios greater than 3.6. At  $J = 3.8$  and  $C_p = 1.0$ , however, the efficiency of propeller 55D (slightly more than 89.5 percent) is only about 1.5 percent better than that of propeller 30D (about 88 percent). In reference 5, at  $J = 3.8$  and  $C_p = 0.5$ , the rear component only of propeller 55D (propeller 55S) showed an efficiency of about 91 percent, whereas the efficiency of the rear component only of propeller 30D (propeller 30S) was about 83 percent, a difference of 8 percent. The small advantage in efficiency of the high-pitch dual-rotating propeller is in sharp contrast with the definite advantage that occurs in the case of single-rotating propellers at high advance ratios.

Figure 15 gives a comparison of the experimentally determined efficiencies of propellers 30D and 55D for various operating conditions. Figure 15(a) shows the efficiency variation at  $C_p = 0.2$  for a range of low values of  $J$  representative of the take-off range. Figure 15(b) shows the efficiency variation at  $C_p = 0.5$  for a range of medium values of  $J$  representative of the climbing range. The efficiency variation is also shown at  $C_p = 0.7$  for values of  $J$  representative of the high-speed range (fig. 15(c)). Very little difference is shown in the propeller efficiencies at any given condition of  $J$  and  $C_p$ . Similar comparisons of propellers 30S and 55S (fig. 23 in reference 5) showed appreciable differences in efficiency in the climb and high-speed ranges but very little difference occurred in the take-off range.

From figure 15 are selected several conditions to serve as a basis for an analysis and comparison of the energy losses due to lift and profile drag. In propeller operation at constant power, the power coefficient varies with changes in altitude. Thus, if  $C_p = 0.2$  represents operation at sea level,  $C_p = 0.5$  represents operation at approximately 28,000 feet and  $C_p = 0.7$  represents operation at about 36,750 feet. Values of  $J$  are accordingly selected to represent the appropriate flight condition, that is, take-off at sea level, climb at an intermediate altitude, and high speed at altitude. The propeller calculations are not sufficiently extensive to permit comparison at exactly the same value of  $J$  for both propellers; accordingly, the analysis and comparison are based on the following conditions of  $C_p$  and  $\beta_F$ :

Flight condition	$\rho/\rho_0$	$C_p$	$\beta_F$	Propeller 30D		Propeller 55D	
				$J$	$\eta$	$J$	$\eta$
Take-off at sea level	1.0	0.2	$30^\circ$	1.04	0.845	0.96	0.800
Climb at 28,000 feet	.4	.5	$45^\circ$	1.80	.870	1.64	.820
High speed at 36,750 feet	.286	.7	$55^\circ$	2.89	.905	2.68	.890

Because of the differences in  $J$  at each blade angle in the foregoing table, the efficiencies are not directly comparable. At equal values of  $J$  the efficiencies are as follows:

Propeller	Take-off			Climb			High speed		
	$J$	$C_p$	$\eta$	$J$	$C_p$	$\eta$	$J$	$C_p$	$\eta$
30D	0.96	0.2	0.828	1.64	0.5	0.842	2.68	0.7	0.900
55D	.96	.2	.800	1.64	.5	.820	2.68	.7	.890
30D	1.04	.2	.845	1.80	.5	.870	2.89	.7	.905
55D	1.04	.2	.820	1.80	.5	.850	2.89	.7	.900

The comparisons in the preceding table show the correct differences in the efficiencies of the two propellers. The maximum difference is less than 3 percent for any of these conditions.

Load distribution.— The thrust and torque distributions for the operating conditions selected for analysis are shown in figures 16 and 17. The loadings follow the same general trends found in the tests of the single-rotating rear components of these propellers. In the case of propeller 55D, the load over

the outer half of the blade is much greater than that over the inner half at any of the conditions considered. The distributions of  $c_l$  (fig. 18) serve to emphasize the lighter loads of the shank sections of this propeller. The shanks would be expected to take a somewhat larger share of the load for propeller operation at values of  $J$  greater than 3.0, but this increase would not be very large for practical values of  $J$ .

The thrust- and torque-gradient curves for propeller 30D show that the shanks take a progressively larger share of the load as  $J$  is increased. The results in figures 16 and 17 show that at  $J = 2.89$  this propeller also carries a very high tip load as compared with that at the midsections. This high tip load is the result of insufficient twist of the outer radii for operation at high values of  $J$ , and the tip loads would be expected to become still higher with respect to the midsections at higher values of  $J$ . The fact that the tip load of the front component is always less than that of the rear component is not surprising because the blade-twist curves in figure 4 show that the outer radii of the front component have almost as much twist as those of propeller 55D.

#### Analysis of Energy Losses

Data from the load-gradient curves in figures 16 and 17 have been used to evaluate the energy losses  $\frac{E_a}{P}$ ,  $\frac{E_r}{P}$ , and  $\frac{E_D}{P}$  by means of equations (2) to (4). The results are presented in table I. The quantity  $\frac{E_r}{P}$  was found to be negligibly small and for this reason is omitted. These rotational energy losses are discussed more fully in a subsequent section.

As pointed out previously, the efficiency of one propeller is not directly comparable with the efficiency of the other because of the differences in  $J$ . In general, however, a decrease in  $J$  requires increased values of  $c_l$  to maintain the same value of  $C_p$  at a given altitude. Thus, the differences in  $\frac{E_a}{P}$  between the two propellers at the climb and high-speed conditions are somewhat greater than those that occur at equal values of  $J$ . The tabulated values show reasonably good agreement between observed and calculated efficiencies. The quantity  $\frac{E_a}{P} + \frac{E_D}{P}$  should equal  $1 - \eta$  if all losses are accounted for, and reasonable agreement is obtained in this respect.

Axial energy loss.— The distribution of the axial energy loss  $aV dT$  in nondimensional form is shown for each operating condition in figures 19 and 20. In table I is given the value of  $E_a/P$  for each condition. The values of  $E_a/P$  for propeller 30D are always less than the values for propeller 55D at the same values of  $C_p$  and blade-angle setting. The maximum difference (0.028) indicated in table I occurs in the climbing range. This difference is not unduly large and would be smaller if both propellers operated at the same advance ratio.

Rotational energy loss.—The rotational-energy-loss calculations gave values of  $E_r/P$  that did not exceed 0.001, or one-tenth of 1 percent, for any of the conditions considered. Such complete recovery of this loss cannot be expected with propellers of finite numbers of blades. The actual recovery rate is uncertain and probably depends on the number of blades in each component.

The comparison of values of  $\frac{E_a + E_D}{P}$  with the observed values of  $1 - \eta$  in table I indicates discrepancies up to about 0.03. It is probable that the rotational loss exceeds the calculated value but is within the limits between the measured and calculated energy losses shown in table I.

Profile-drag energy loss.—The profile-drag energy loss at each section depends on  $\gamma$  and the resultant air-stream angle  $\phi$  as shown in equation (5). At values of  $\phi$  between approximately  $20^\circ$  and  $70^\circ$ , however, the loss is relatively independent of  $\phi$  and is almost directly proportional to  $\tan \gamma$  alone. Efficient airfoil sections have a fairly large range of lift coefficients for which values of  $\tan \gamma$  are small.

Distributions of the profile-drag losses for the flight conditions of table I are shown in figure 21. For most of these cases, the resultant angle  $\phi$  is within the range of  $20^\circ$  to  $70^\circ$  at all sections. The two propellers show large peaks in the drag-loss distributions for the climb conditions. The distributions of  $c_l$  for climb in figure 18 show high values of  $c_l$  which are conducive to high values of  $\tan \gamma$  (fig. 2(b)). These high values of  $c_l$  are seen to occur over the sections of the blades which produce high values of  $(1 - \eta'_0) \frac{dC_Q}{dx}$  (fig. 21).

In the high-speed condition the curves show large drag losses in the shank regions of propeller 30D. The values of  $c_l$  are high but are short of the range in which abrupt increases in  $\tan \gamma$  occur. The resulting moderate values of  $\tan \gamma$ , however, occur in a region in which the aerodynamic helix angles are near or slightly greater than  $70^\circ$ ; this fact accounts for the large profile-drag losses shown.

The midsections of propeller 30D carry low values of  $c_l$  with respect to the shank and tip sections at  $J = 2.89$ . This distribution would be aggravated at higher values of  $J$ . Such a distribution is poor because at high power coefficients the shanks and tips operate in the stall region which gives high values of  $\tan \gamma$ , and at low power coefficients the midsections operate near  $c_l = 0$ , which again results in high values of  $\tan \gamma$ . The midsections and tip sections of propeller 55D are better suited to a wide range of power coefficients at high speed because values of  $c_l$  are such that both the stall at high power coefficients and unloading at low power coefficients occur more uniformly. Thus, at a given value of  $J$  in the high-speed range propeller 55D would be expected to maintain high efficiency over a larger range of power coefficients than propeller 30D.

For example, figure 8 shows that at  $J = 3.8$  the efficiency of propeller 55D is greater than 87.5 percent through a range of  $C_p$  from 0.53 to 1.425. The efficiency of propeller 30D, however, is greater than 87.5 percent through the smaller range of  $C_p$  from 0.76 to 1.31 at the same value of  $J$  (fig. 10).

### Design Considerations

The design of a dual-rotating propeller is complicated by the lack of a well-established design procedure. The design procedure for optimum single-rotating propellers requires a progressive unloading of the shank sections in accordance with the minimum-energy-loss distribution as the design value of  $J$  is increased. This progressive unloading of the shank sections is required to minimize the rotational energy loss. Such a procedure is not necessary in the case of dual rotation because the rotational loss is largely recoverable for conversion into added thrust. Hence, more of the load can be carried inboard at high advance-diameter ratios. Since complete recovery of the rotational loss cannot be expected, some limit exists as to the amount the shanks can be loaded without penalty.

It is of interest to compare the induced losses only of propellers 30D and 55D with the induced loss of a six-blade single-rotating propeller having the minimum induced-energy-loss load distribution and, also, with that of an ideal actuator disk. The induced losses for these propellers are simply  $\frac{E_a}{P}$  (on the assumption that  $\frac{E_r}{P}$  is negligible as calculated).

The minimum induced loss  $\left(\frac{E_a + E_r}{P}\right)_{\text{opt}}$  of single-rotating propellers is obtained from the charts of reference 7 and is further arranged to show these two losses separately. The induced energy loss of an ideal actuator disk  $\left(\frac{E_a}{P}\right)_1$  is given in reference 8. These losses have all been determined for the conditions in table I and are shown in table II.

Values of  $\left(\frac{E_a}{P}\right)_{\text{opt}}$  are not a great deal higher than  $\left(\frac{E_a}{P}\right)_1$  for the range of operating conditions considered. Thus, if the rotational loss is canceled, the use of the Betz optimum single-rotating-propeller load distribution should result in nearly the best efficiency possible for dual-rotating propellers. The small difference in values of  $\left(\frac{E_a}{P}\right)_{\text{opt}}$  and  $\left(\frac{E_a}{P}\right)_1$  is especially noteworthy because the results in table II cover a range of ideal-actuator-disk efficiencies from 90 percent to nearly 100 percent (or in other words, medium to light power loadings).

The required concentration of blade loading over the outer radii specified in the Betz loading at the higher values of  $J$ , however, brings up compressibility considerations, inasmuch as these heavy loads occur in

the region of highest Mach numbers. Cases may thus arise in which physical limitations on the propeller dimensions might require operation at values of  $c_l$  in the critical range. If the load is arbitrarily shifted inward for single-rotating propellers, compressibility losses at the tip are decreased at the expense of increased rotational losses. The good efficiency of propeller 30D with high shank loadings as compared with that of propeller 55D with a loading approaching the Betz distribution in the high-speed range indicates that the load may be shifted away from the tip with no adverse effect on the induced efficiency of dual-rotating propellers. This inward shift of the load may even be beneficial to the over-all efficiency, although the comparison between  $\left(\frac{E_a}{P}\right)_1$  and  $\left(\frac{E_a}{P}\right)_{opt}$  in table II indicates that no significant gain is to be anticipated.

The results of these tests show that the differences in blade load distribution of propellers 30D and 55D have little effect on the induced efficiency for a wide range of operating conditions. This insensitivity of the induced efficiency to blade load distribution should allow the propeller designer appreciable latitude in controlling the profile-drag losses for dual-rotating propellers.

#### CONCLUSIONS

Tests were made to determine the efficiency at low tip speeds of two 10-foot-diameter six-blade dual-rotating propellers differing only in pitch distribution. The following conclusions are based on the results of these tests supplemented by analytical calculations based on interpolated airfoil data:

1. Satisfactory agreement was obtained between the measured and calculated dual-rotating-propeller characteristics.
2. A dual-rotating propeller of low design pitch maintained high efficiency at advance ratios greater than 2.5 as contrasted with the serious losses resulting from operation of a similar single-rotating propeller in the same range.
3. The induced efficiency of dual-rotating propellers near peak efficiency was relatively independent of blade load distribution.

Langley Memorial Aeronautical Laboratory  
National Advisory Committee for Aeronautics  
Langley Field, Va., February 3, 1948



## REFERENCES

1. Biermann, David, and Hartman, Edwin P.: Wind-Tunnel Tests of Four- and Six-Blade Single- and Dual-Rotating Tractor Propellers. NACA Rep. No. 747, 1942.
2. Lesley, E. P.: Tandem Air Propellers. NACA TN No. 689, 1939.
3. Lesley, E. P.: Tandem Air Propellers - II. NACA TN No. 822, 1941.
4. Naiman, Irven: Method of Calculating Performance of Dual-Rotating Propellers from Airfoil Characteristics. NACA ARR No. 3E24, 1943.
5. Gilman, Jean, Jr.: Wind-Tunnel Tests and Analysis of Three 10-Foot-Diameter Three-Blade Tractor Propellers Differing in Pitch Distribution. NACA ARR No. L6E22, 1946.
6. Stack, John: Tests of Airfoils Designed to Delay the Compressibility Burble. NACA Rep. No. 763, 1943.
7. Crigler, John L., and Talkin, Herbert W.: Charts for Determining Propeller Efficiency. NACA ACR No. L4I29, 1944.
8. Glauert, H.: Airplane Propellers. The Axial Momentum Theory. Vol. IV of Aerodynamic Theory, div. L., ch. II, sec. 3, W. F. Durand, ed., Julius Springer (Berlin), 1935; p. 189.

TABLE I  
 BREAKDOWN OF FRACTIONAL ENERGY LOSSES OF PROPELLERS 55D  
 AND 30D AT VARIOUS FLIGHT CONDITIONS

Propeller	J	Experimental $\eta$	Calculated $\eta$	$\frac{E_a}{P}$	$\frac{E_D}{P}$	$\frac{E_a + E_D}{P}$	Experimental $1 - \eta$
Take-off; $C_p$ , 0.20							
55D	0.96	0.800	0.810	0.136	0.042	0.178	0.200
30D	1.04	.845	.840	.117	.041	.158	.155
Climb; $C_p$ , 0.50							
55D	1.64	0.820	0.802	0.107	0.074	0.181	0.180
30D	1.80	.870	.850	.079	.046	.125	.130
High speed; $C_p$ , 0.70							
55D	2.68	0.890	0.870	0.043	0.039	0.082	0.110
30D	2.89	.905	.890	.031	.050	.081	.095

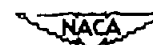


TABLE II

COMPARISON BETWEEN INDUCED LOSSES OF PROPELLERS 30D and 55D,  
 LOSSES OF SIX-BLADE SINGLE-ROTATING PROPELLERS WITH THE  
 BETZ LOADING, AND LOSSES OF AN IDEAL ACTUATOR DISK  
 AT VARIOUS FLIGHT CONDITIONS

Propeller	J	$\frac{E_a}{P}$	$\left(\frac{E_a}{P}\right)_{opt}$	$\left(\frac{E_r}{P}\right)_{opt}$	$\left(\frac{E_a}{P}\right)_i$
Take-off; $C_p$ , 0.20					
55D	0.96	0.136	0.117	0.038	0.102
30D	1.04	.117	.100	.040	.087
Climb; $C_p$ , 0.50					
55D	1.64	0.107	0.072	0.058	0.060
30D	1.80	.079	.065	.055	.045
High speed; $C_p$ , 0.70					
55D	2.68	0.043	0.033	0.055	0.019
30D	2.89	.031	.027	.055	.015



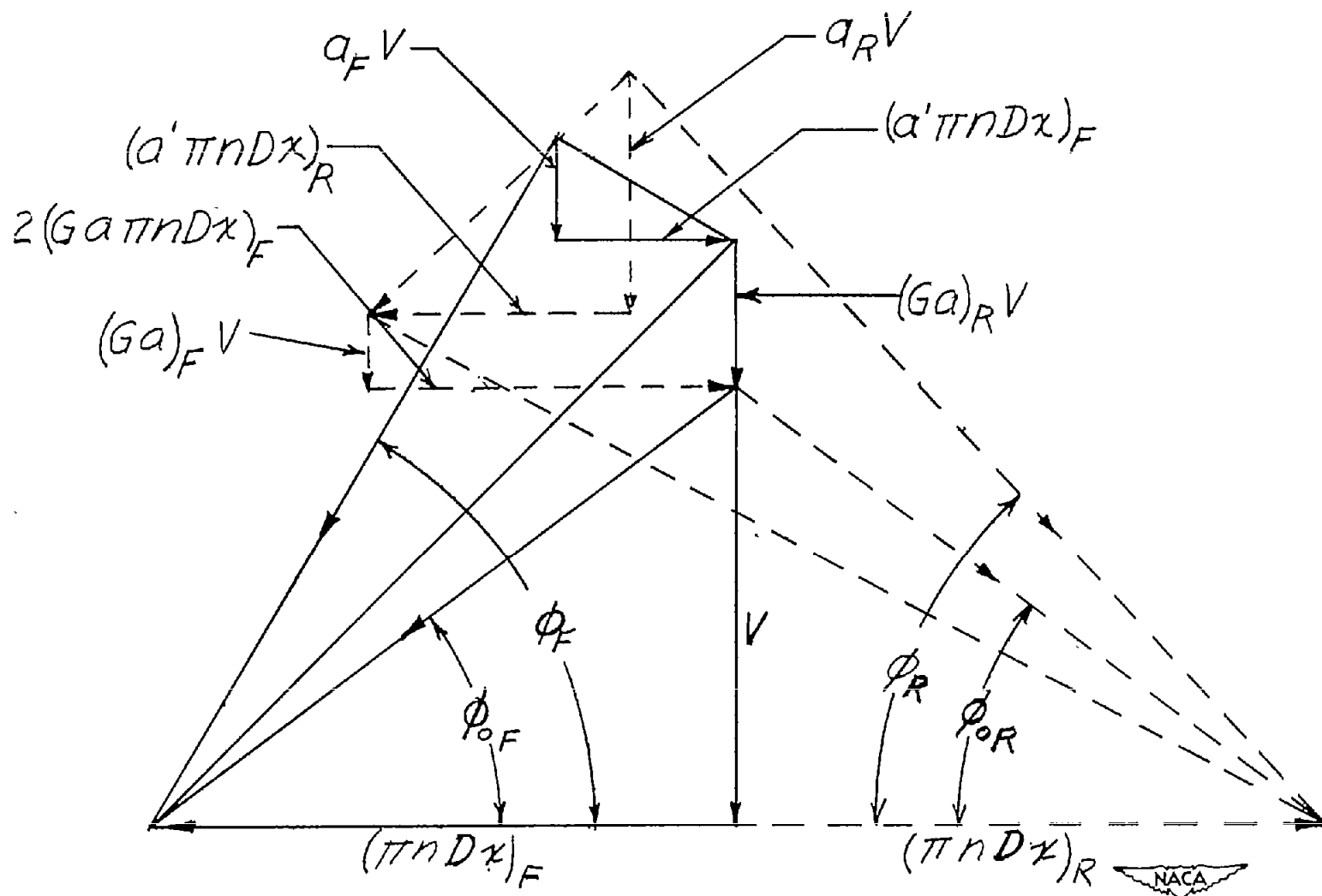
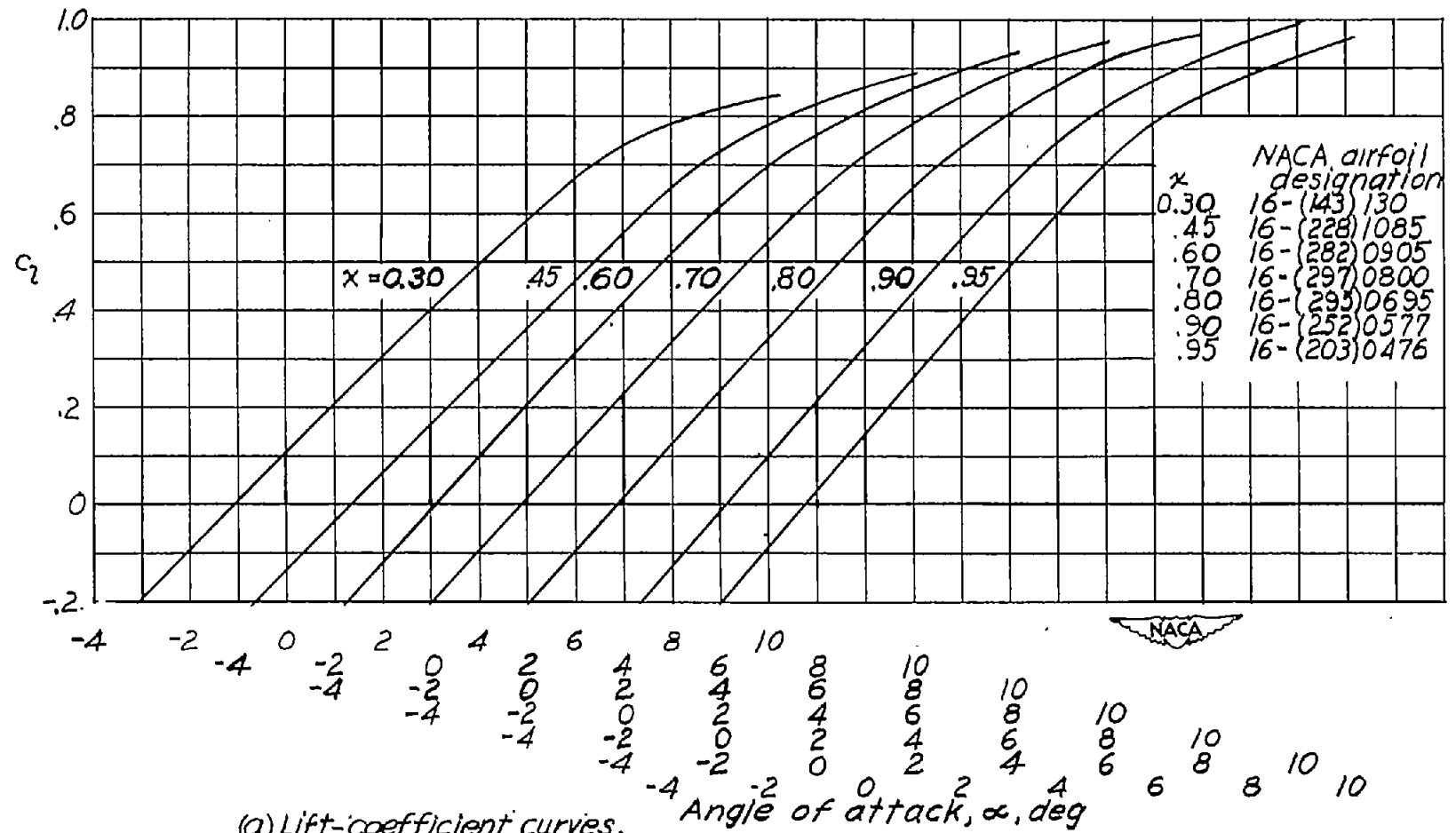
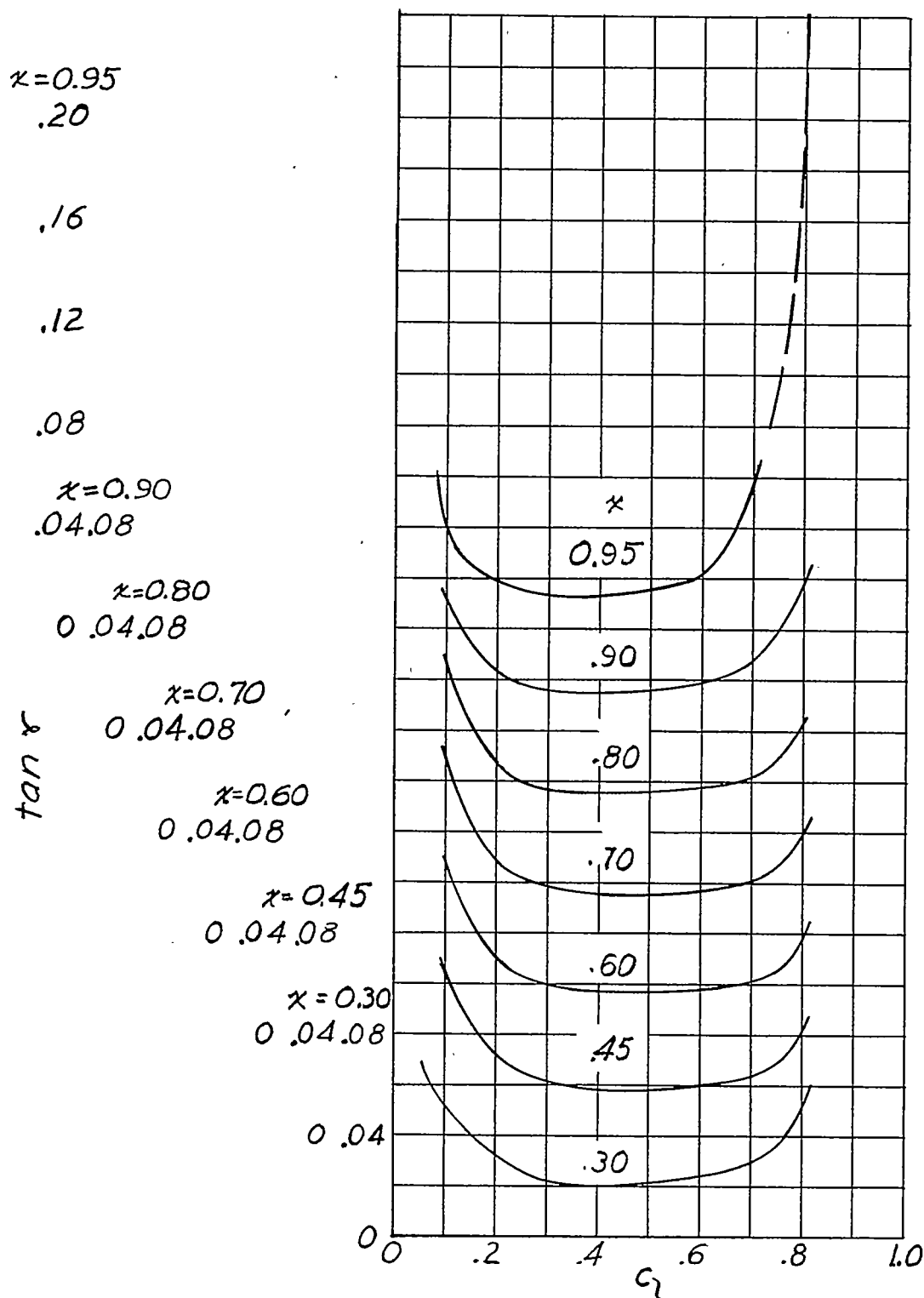


Figure 1.-Velocity diagram for a section of a dual-rotating propeller.



(a) Lift-coefficient curves.

Figure 2.—Two-dimensional airfoil characteristics, NACA 10-(3)(8)-03 propeller sections, Mach number, 0.30.



(b)  $\tan \delta$  curves.

Figure 2.- Concluded.



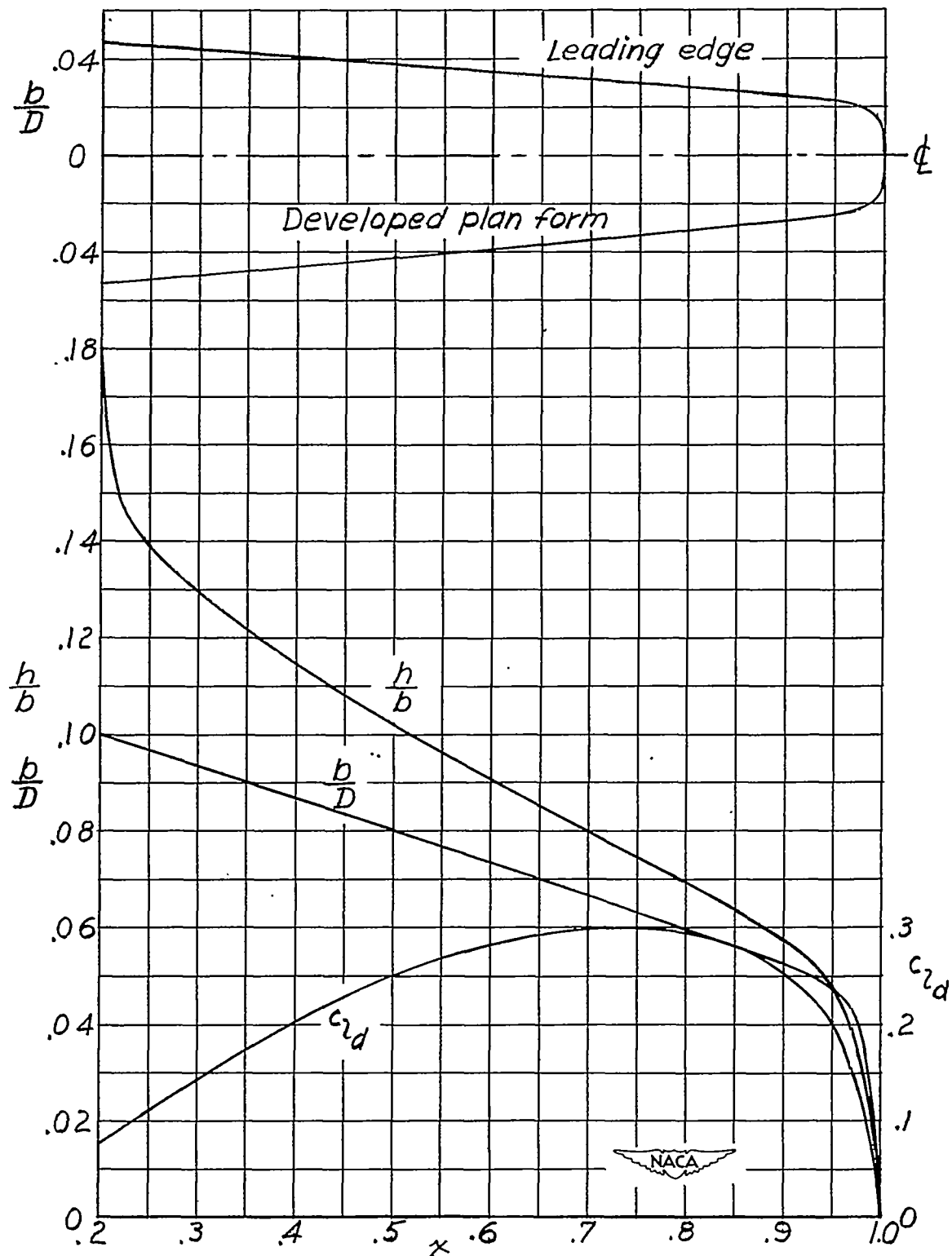


Figure 3. — Blade-form curves and  $c_d$  distribution of NACA propeller 10-(3)(08)-03.

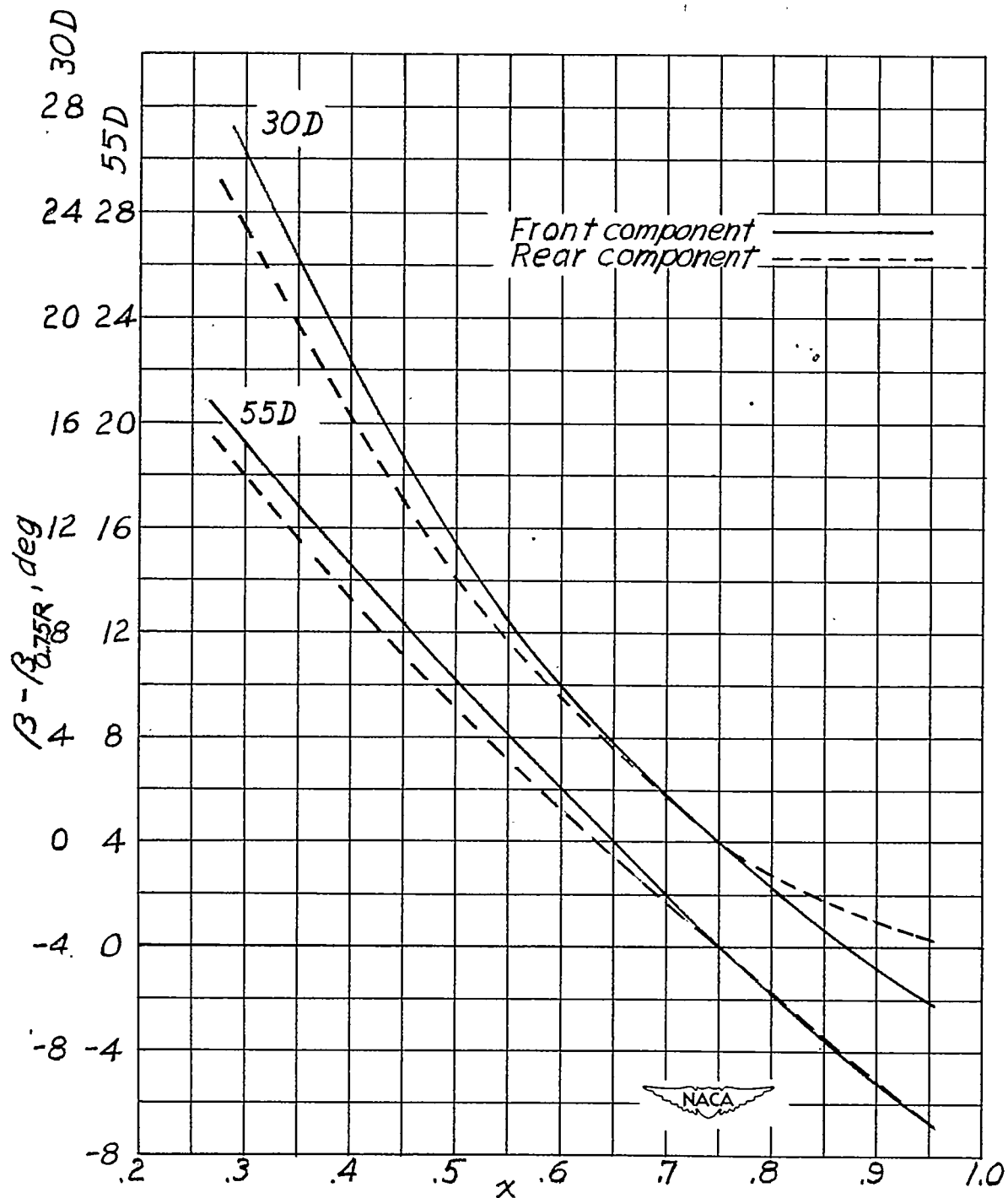


Figure 4. - Blade-angle distribution of front and rear components of propellers 30D and 55D.



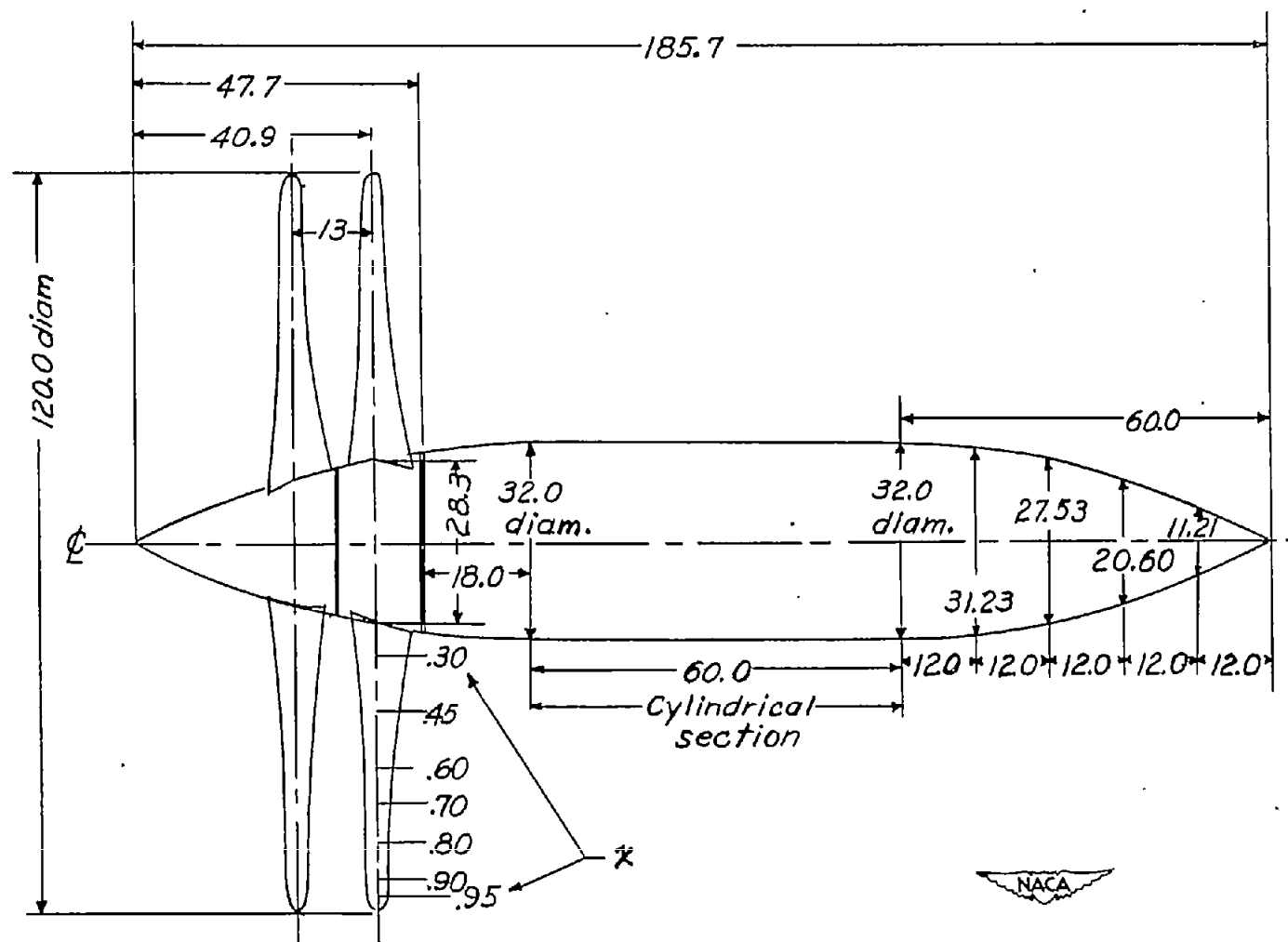


Figure 5.- Dimensional details of test setup. (All dimensions except  $x$  are in inches.)

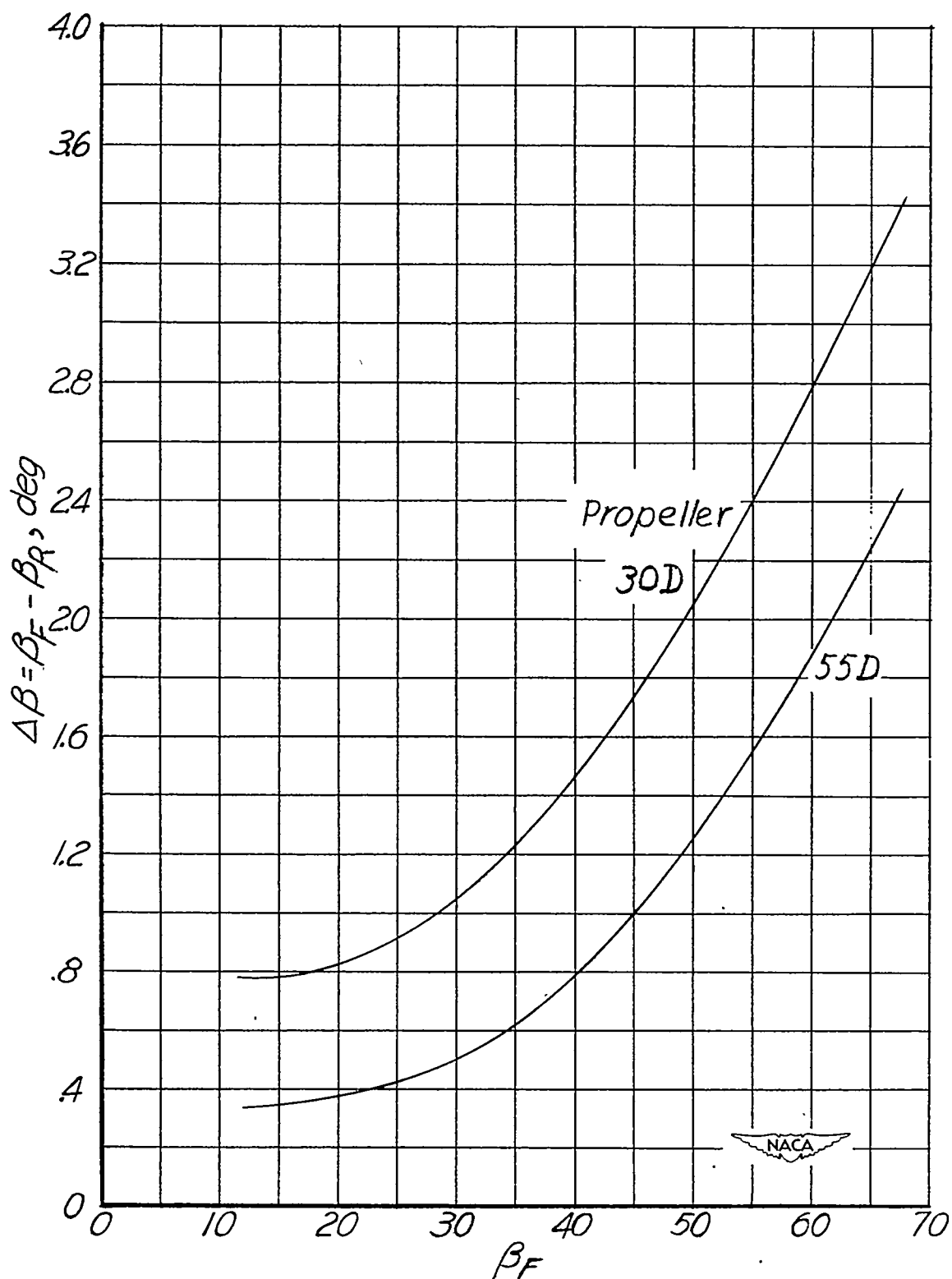


Figure 6.- Curves of  $\Delta\beta$  for six-blade dual-rotating propellers 30D and 55D.

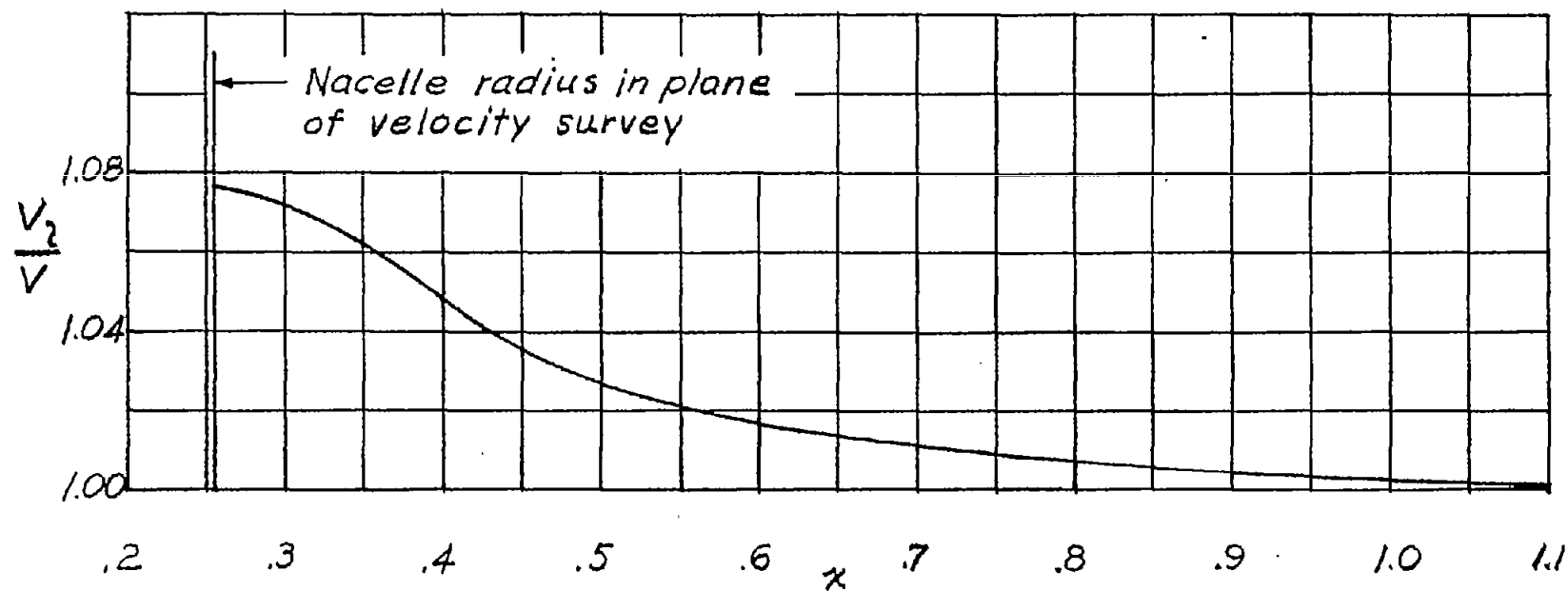


Figure 7.- Velocity distribution  $7\frac{1}{2}$  inches behind rear propeller disk. Propeller removed.



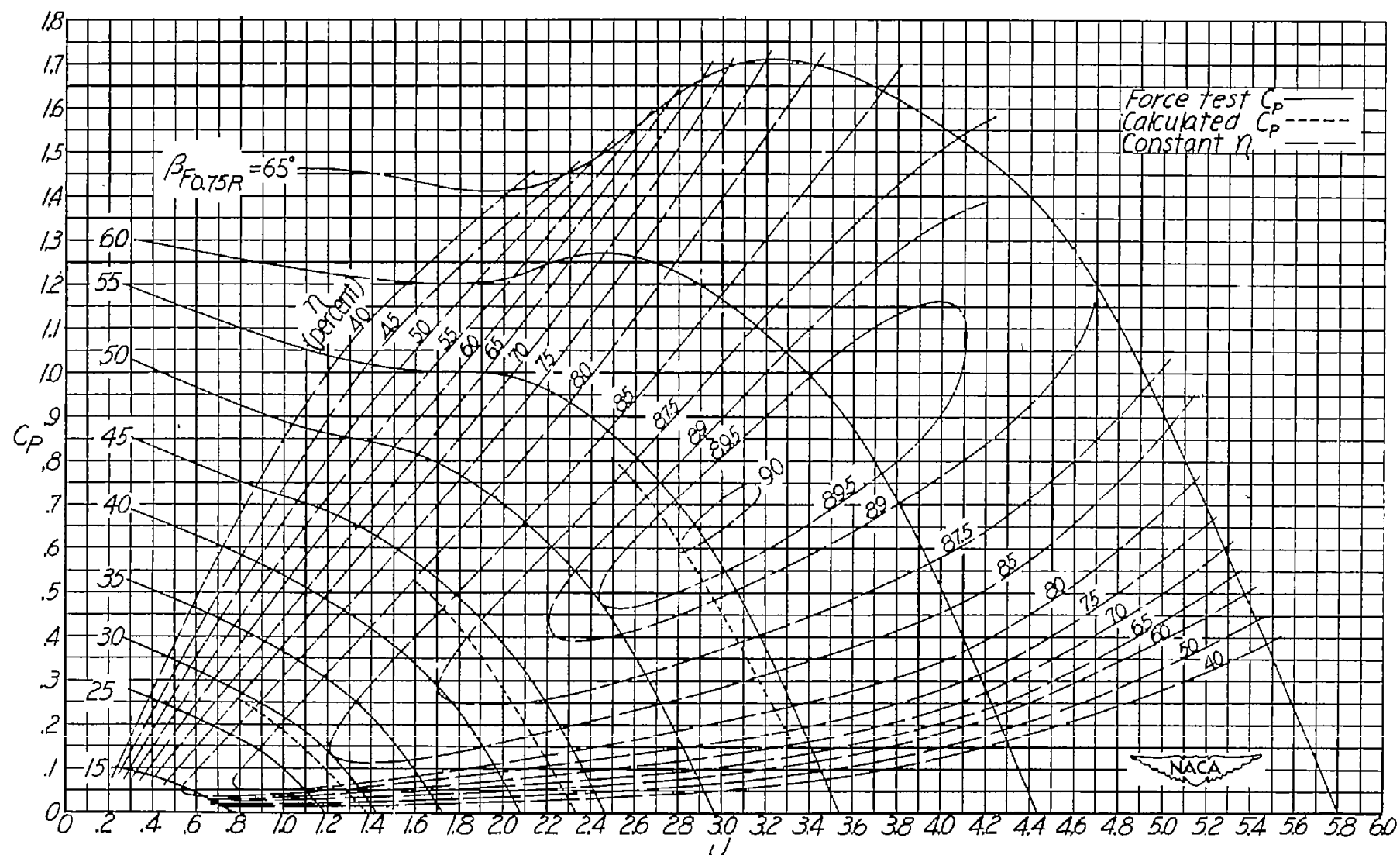
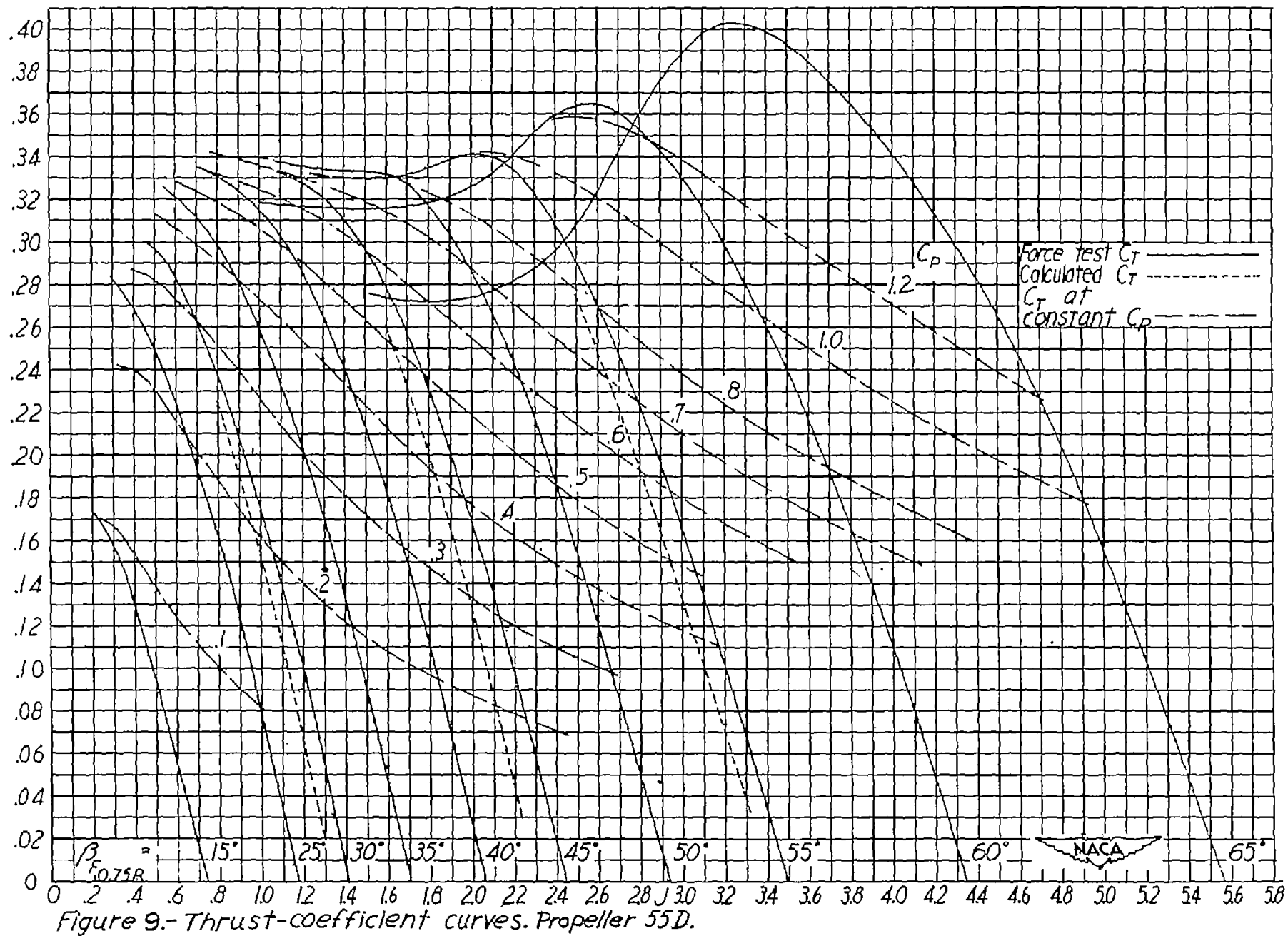


Figure 8.- Power-coefficient and constant-efficiency curves. Propeller 55D.



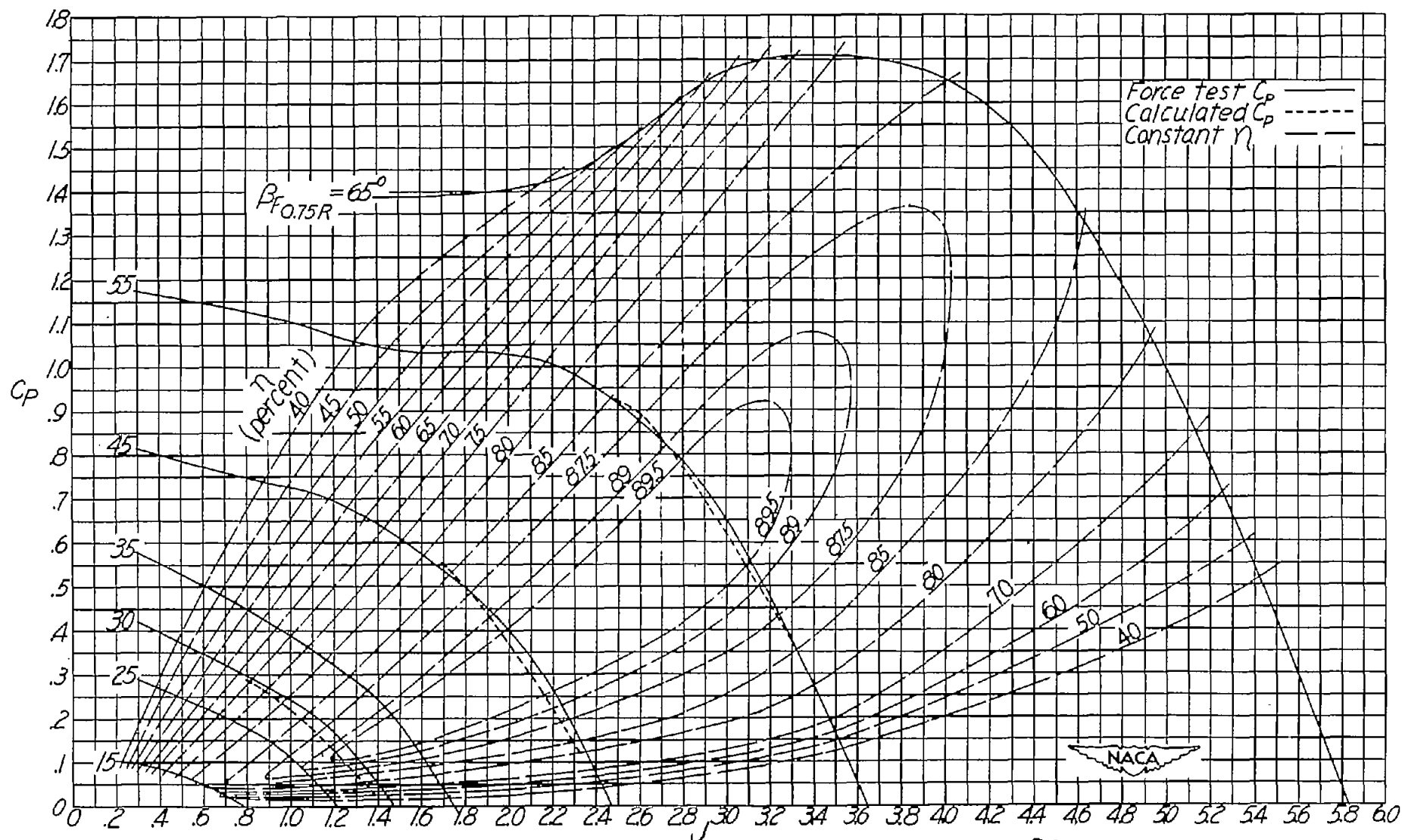


Figure 10.-Power-coefficient and constant-efficiency curves. Propeller 30D.

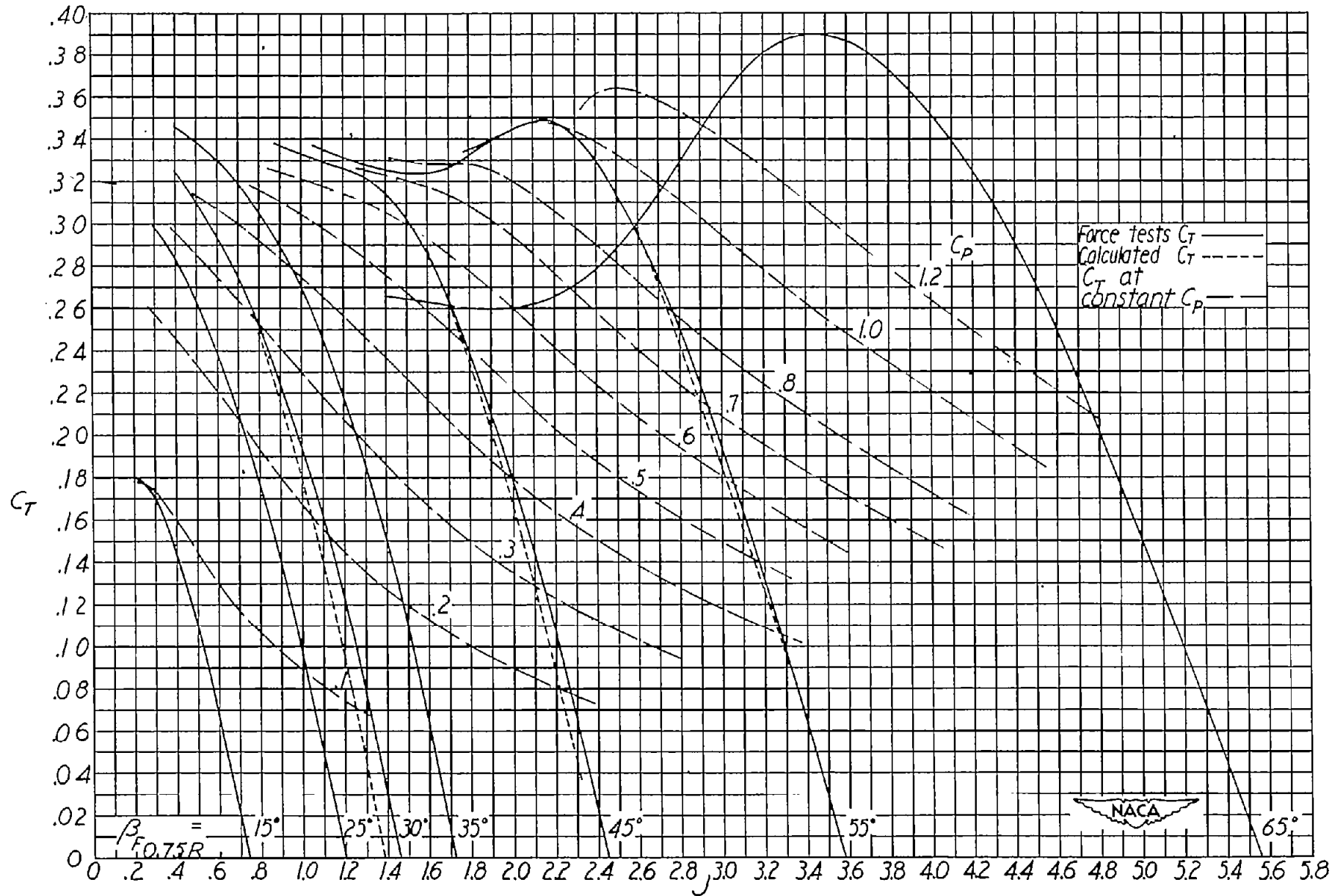
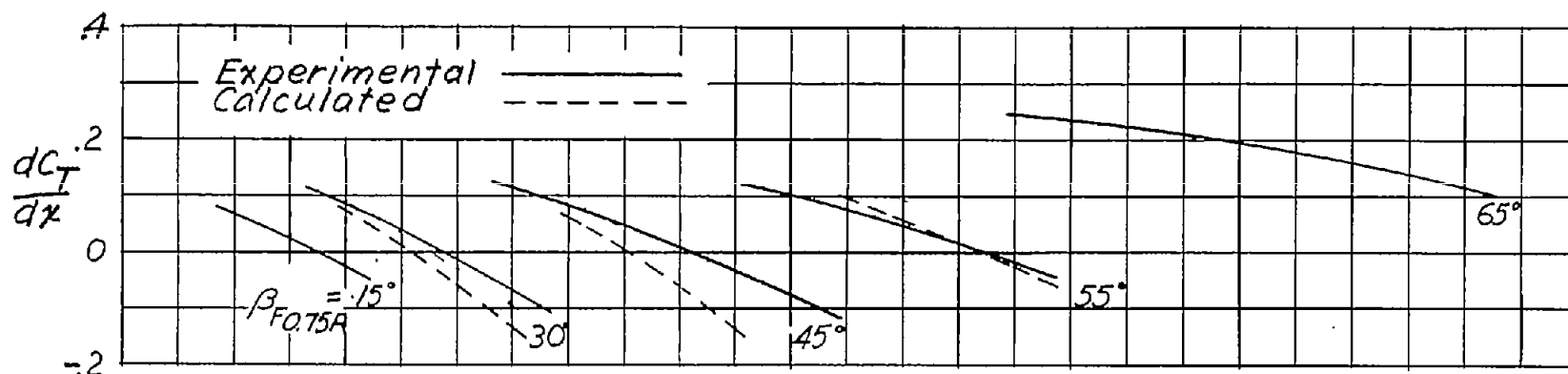
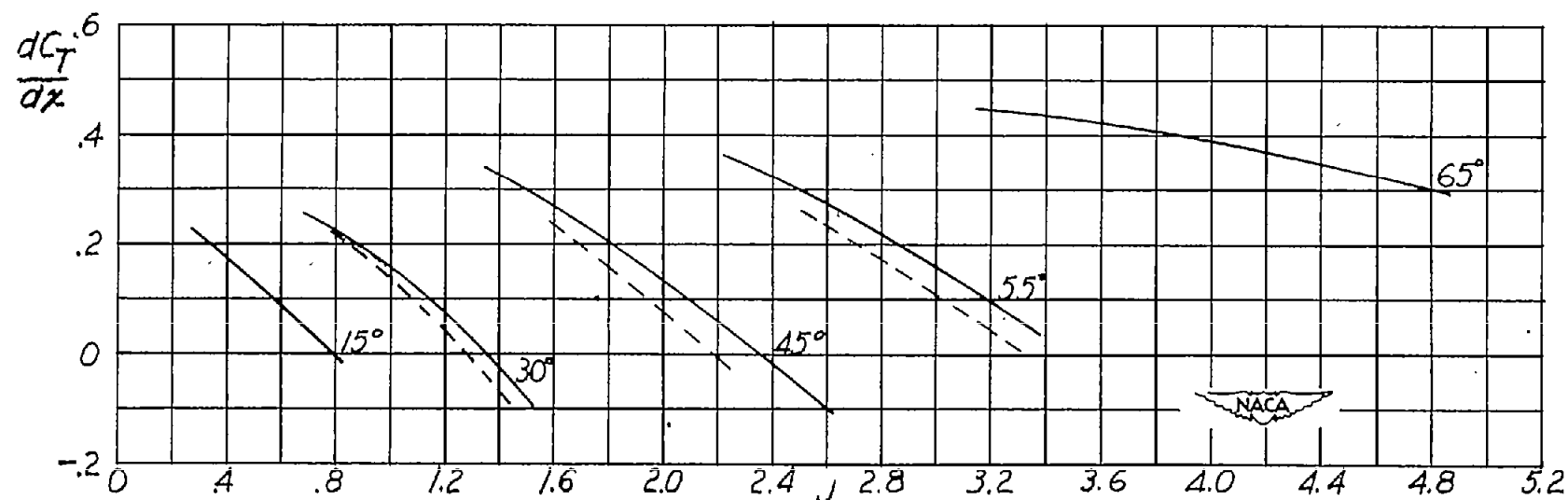


Figure 11.—Thrust-coefficient curves, Propeller 30D.



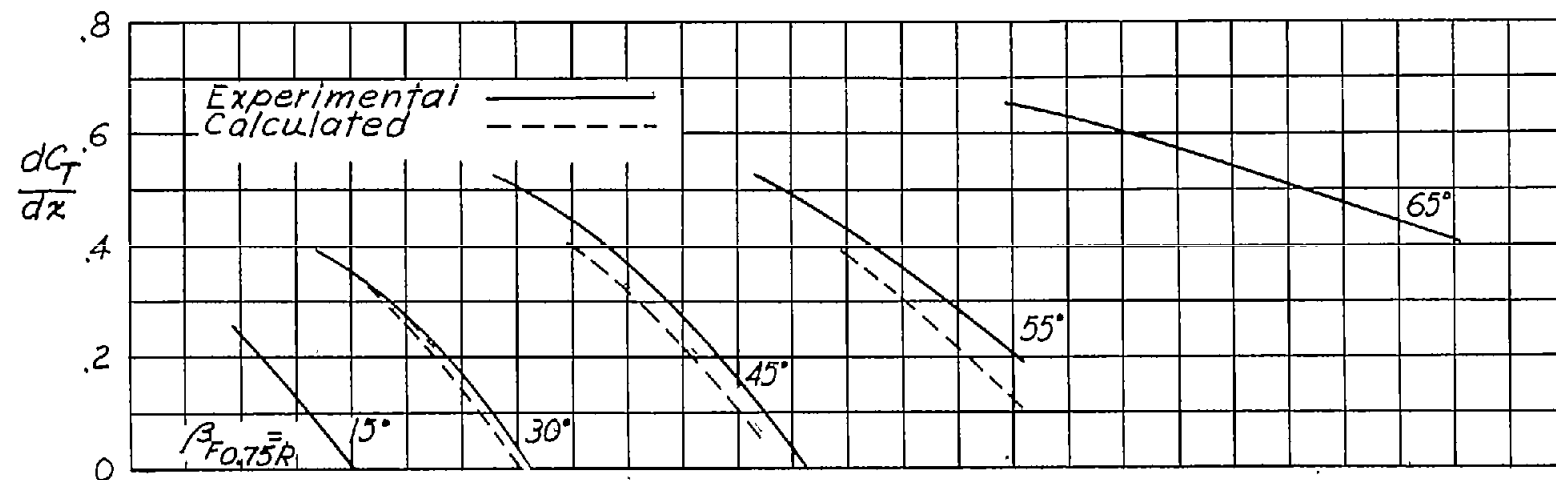
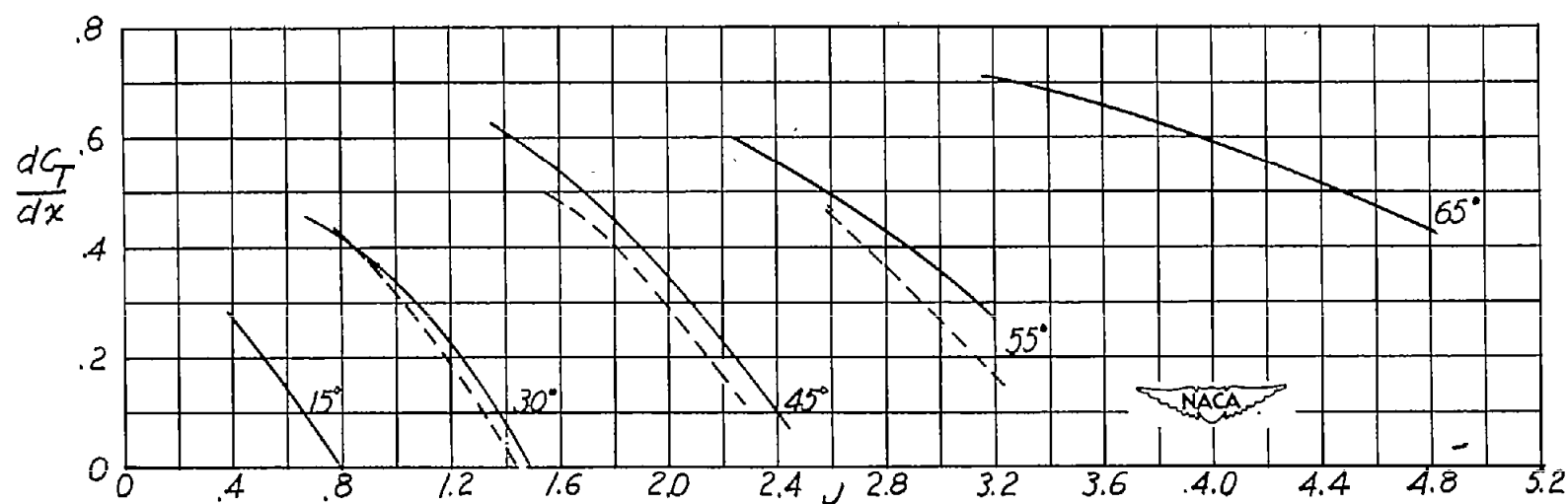
(a)  $x = 0.30$ .

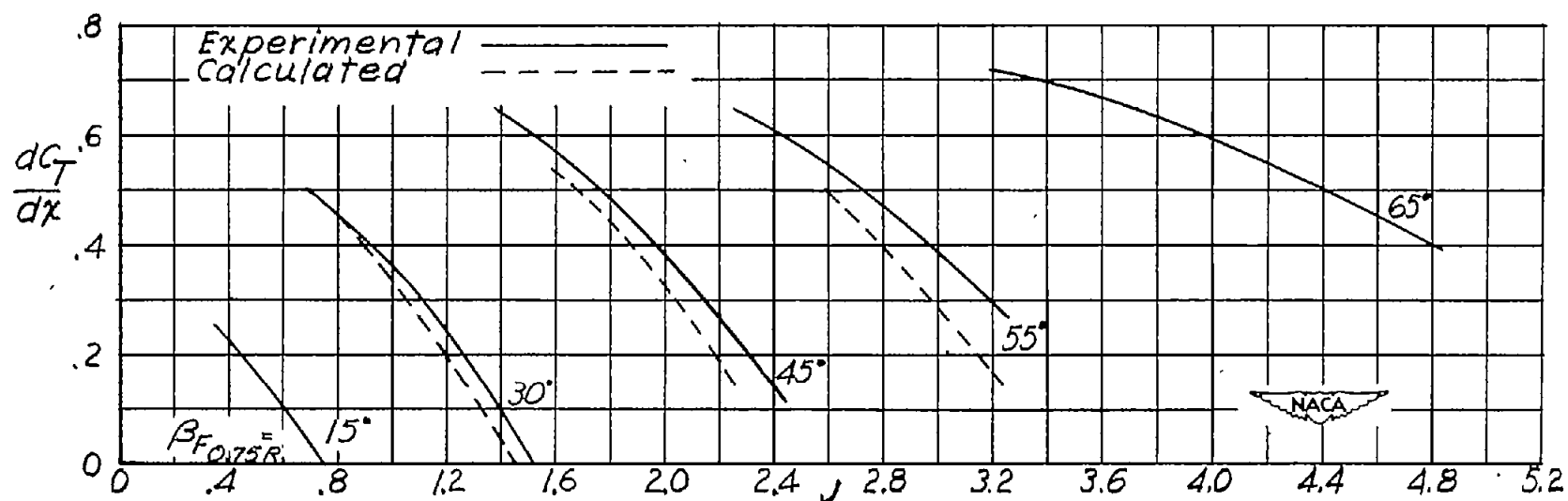


(b)  $x = 0.45$ .

Figure 12.— Blade-section differential thrust coefficients  $\left[ \left( \frac{dC_T}{dx} \right)_F + \left( \frac{dC_T}{dx} \right)_R \right]$  of propeller 55 D.

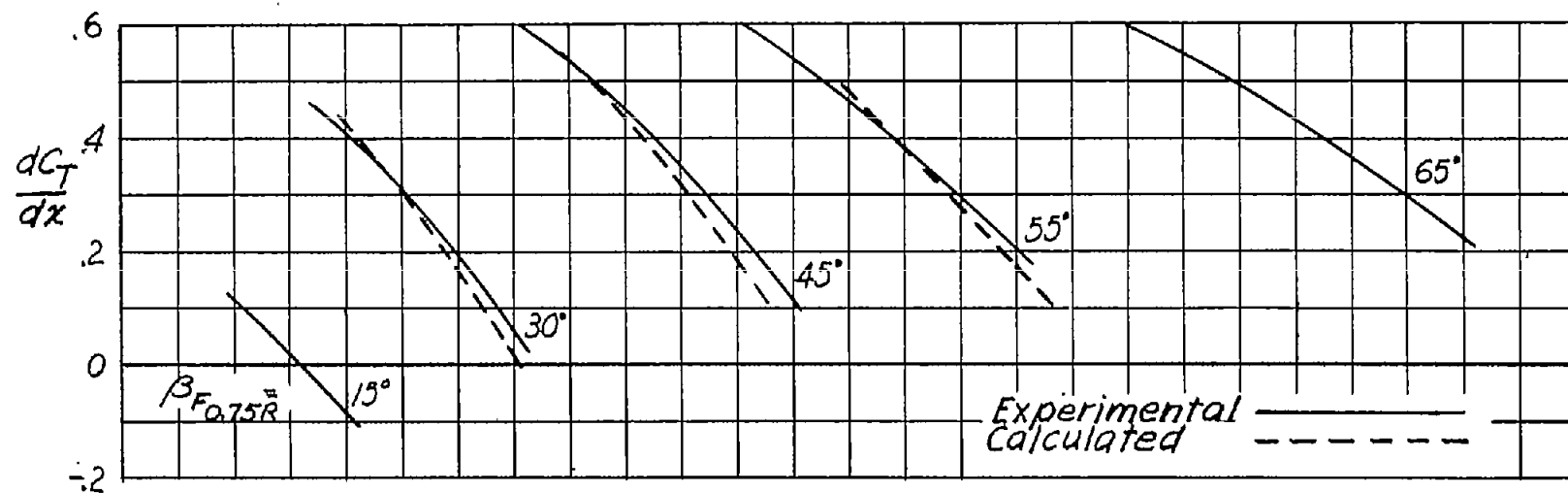


(c)  $\alpha = 0.60$ .(d)  $\alpha = 0.70$ .  
Figure 12.- Continued.

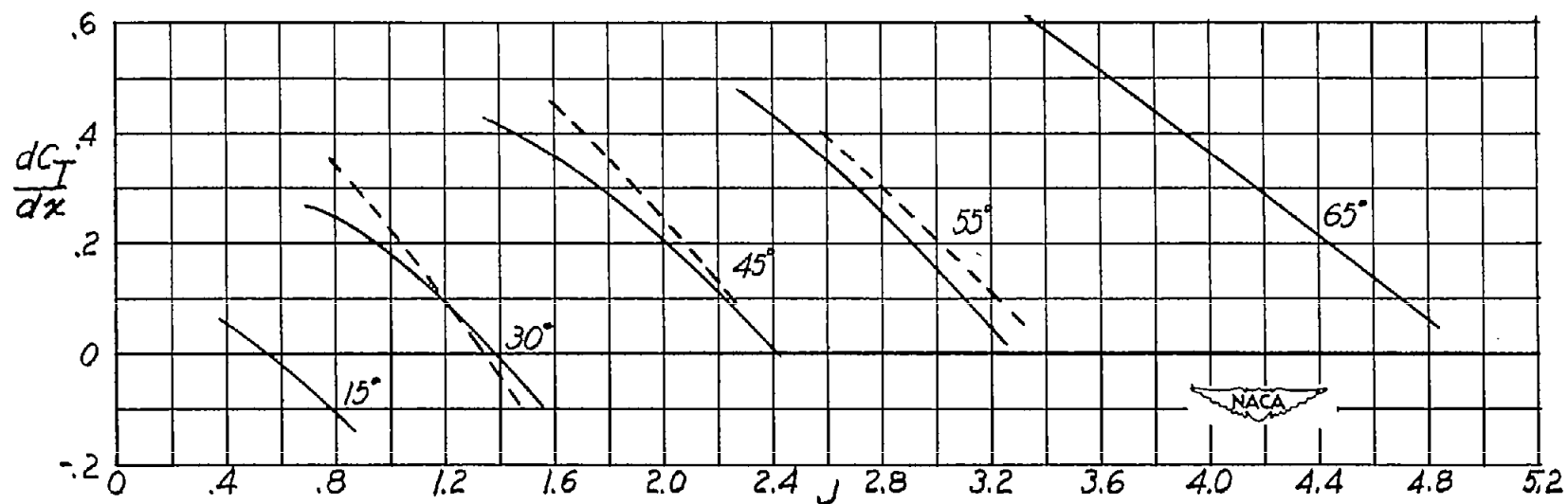


(e)  $\alpha = 0.80$ .

Figure 12.- Continued.



(f)  $x = 0.90$ .



(g)  $x = 0.95$ .  
Figure 2.- Concluded.

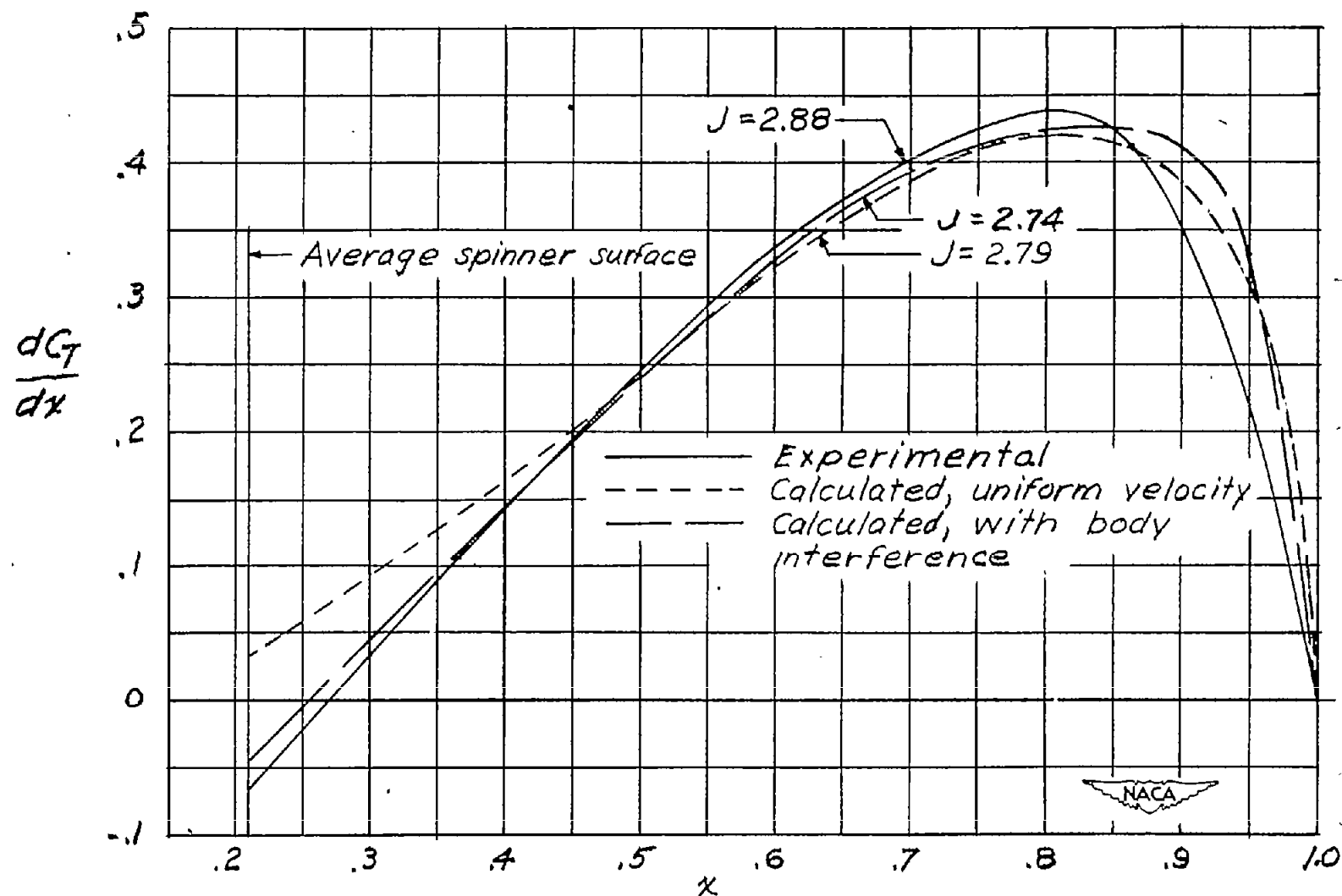
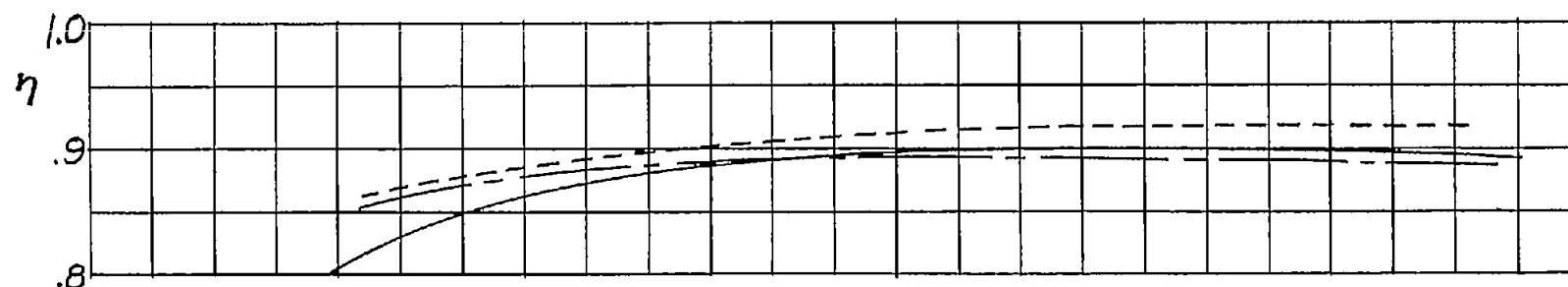
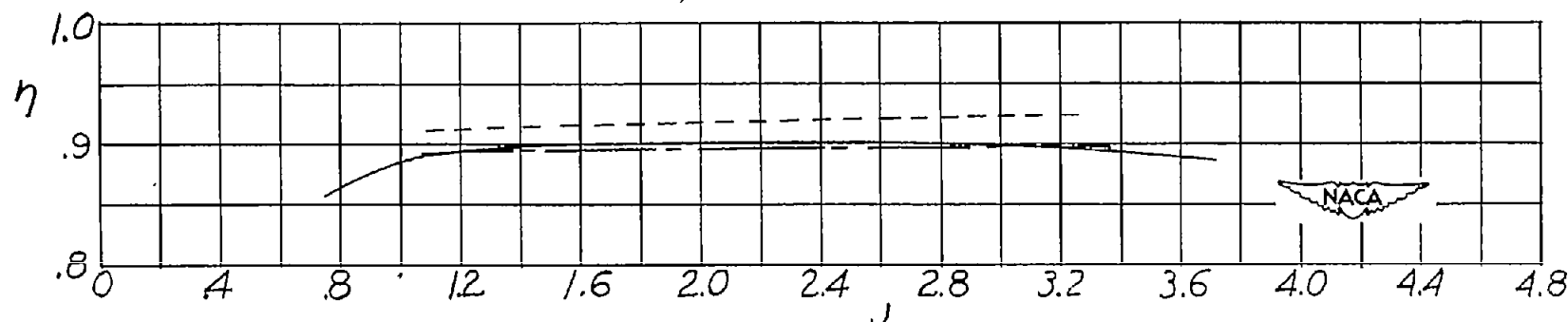


Figure 13.— Comparison of experimental and calculated thrust distribution. Propeller 55D;  $C_p$ , 0.65;  $\beta_F$ ,  $55^\circ$ .

Faired test results —————  
 Calculated, no interference - - - - -  
 Calculated, with interference — — — — —



(a) Propeller 55D.



(b) Propeller 30D.

Figure 14.—Comparison of peak efficiency envelopes derived from faired test data with peak efficiency envelopes calculated with and without body interference.

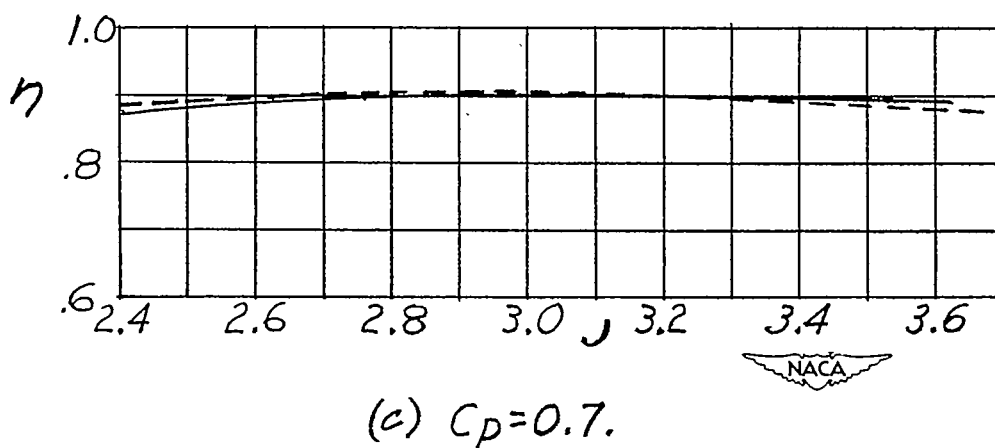
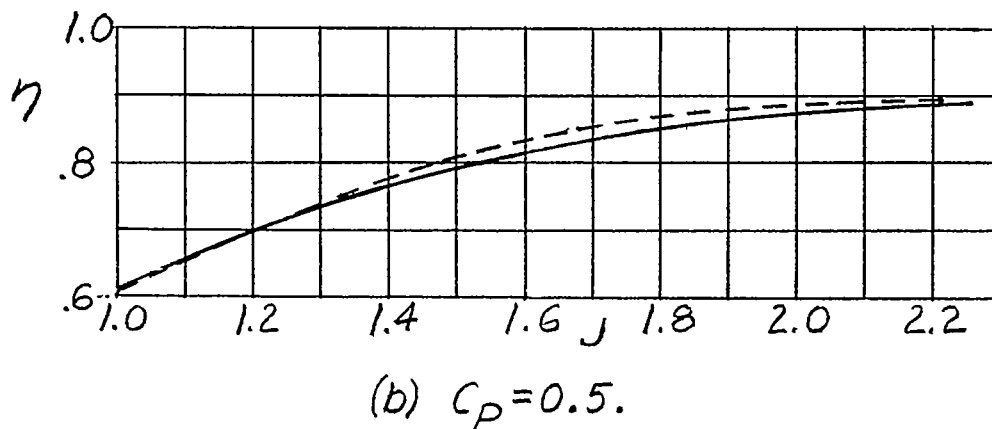
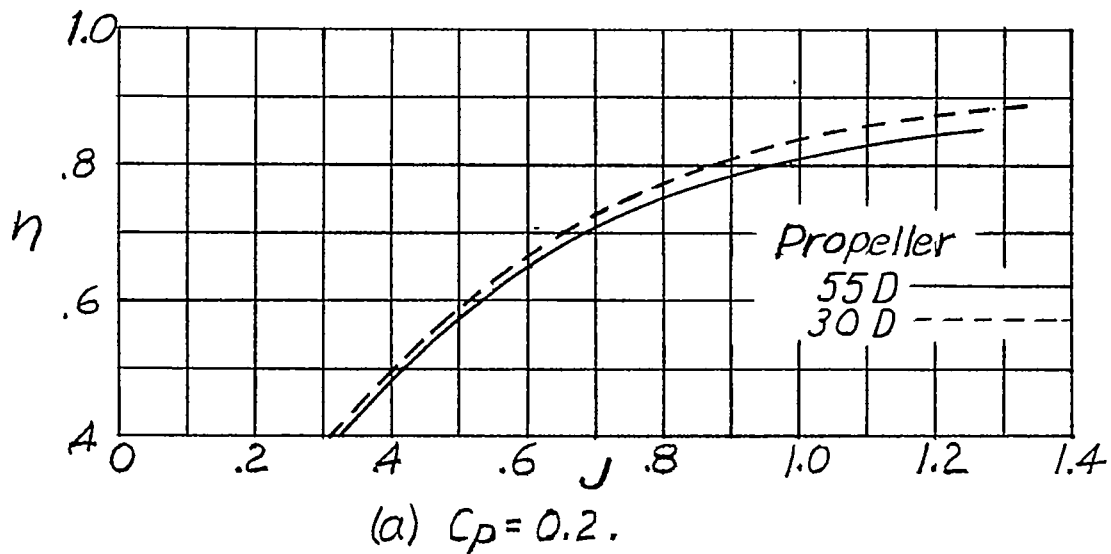
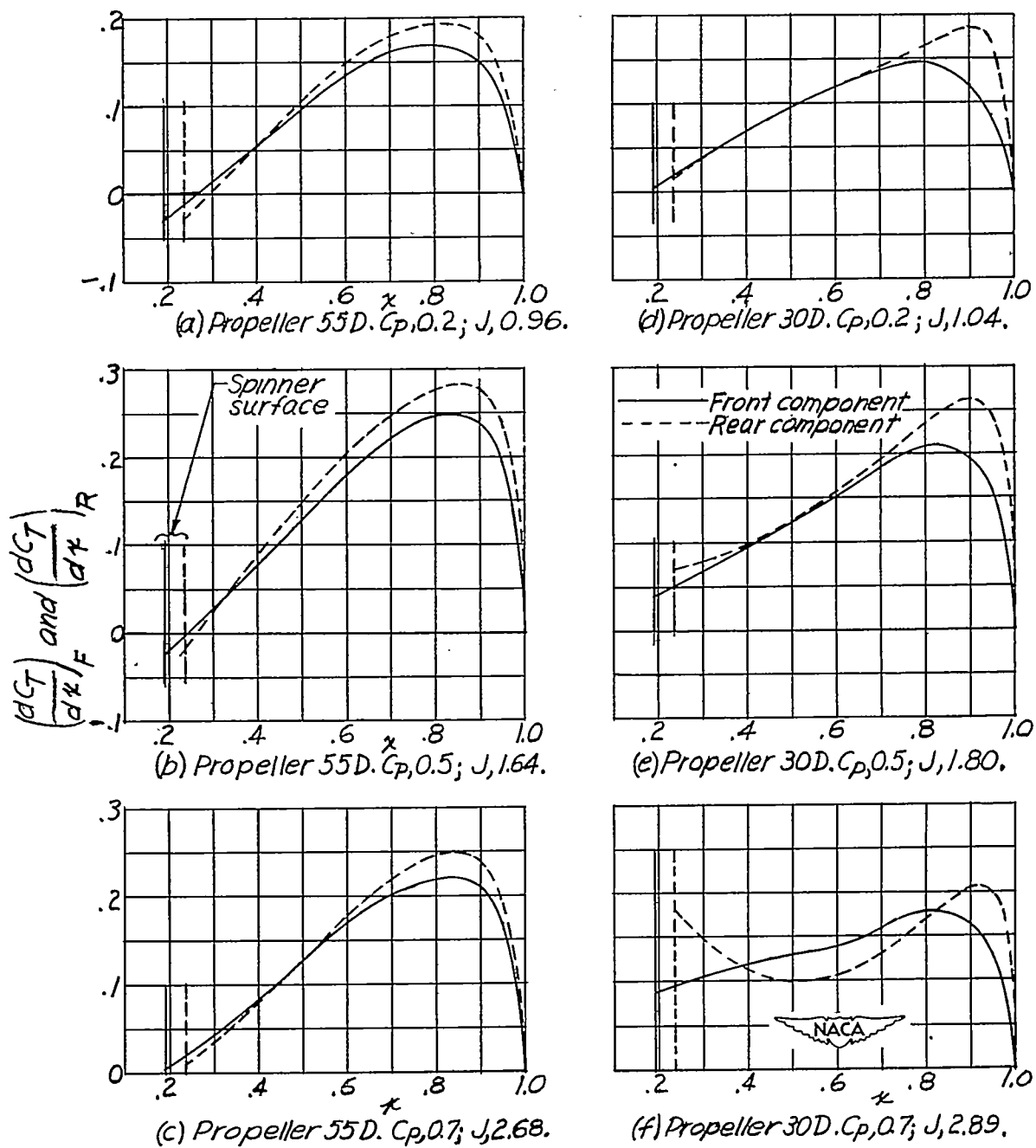
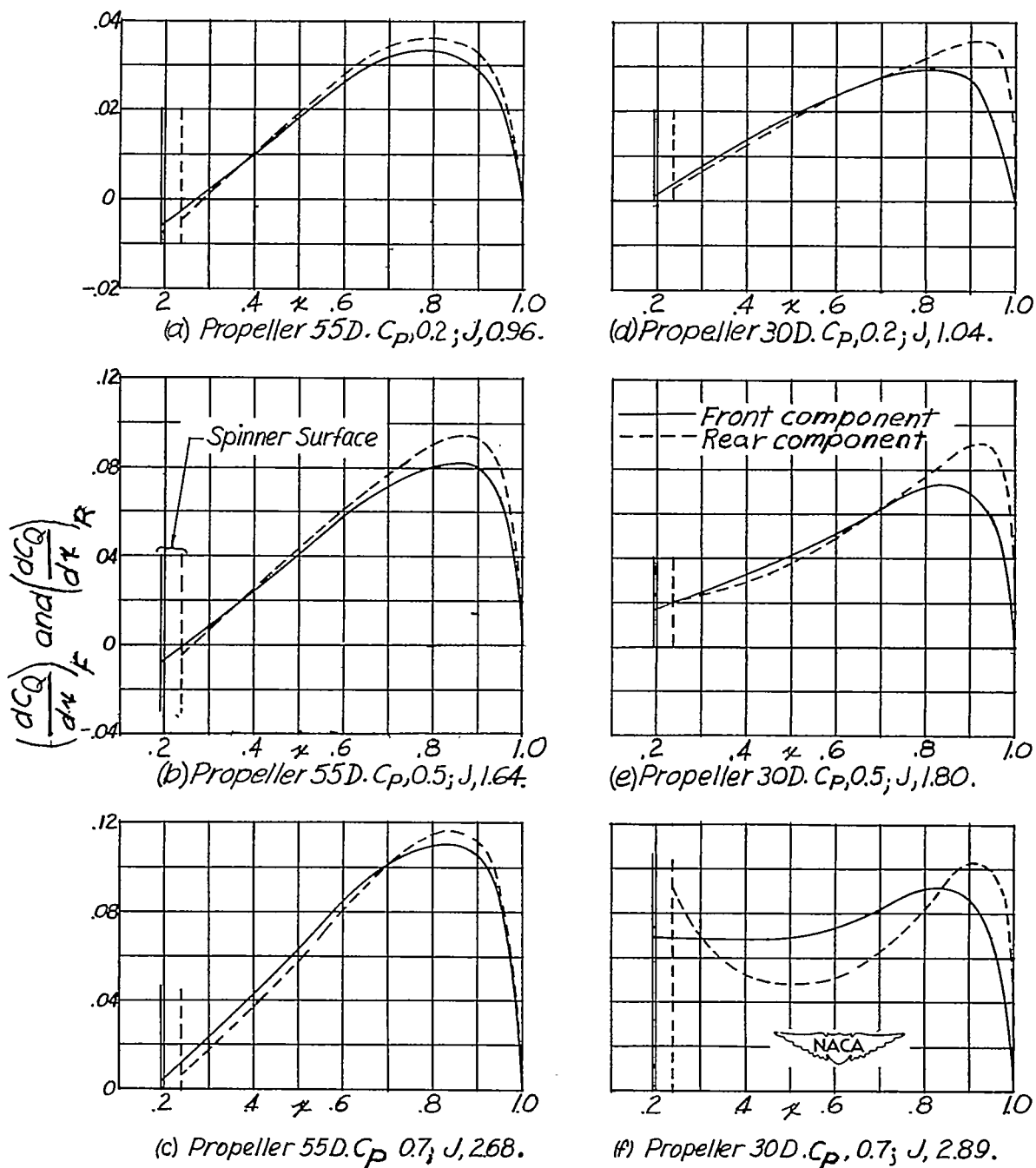


Figure 15.- Variation of  $\eta$  with  $J$  at several constant values of  $C_p$ . Experimental data.







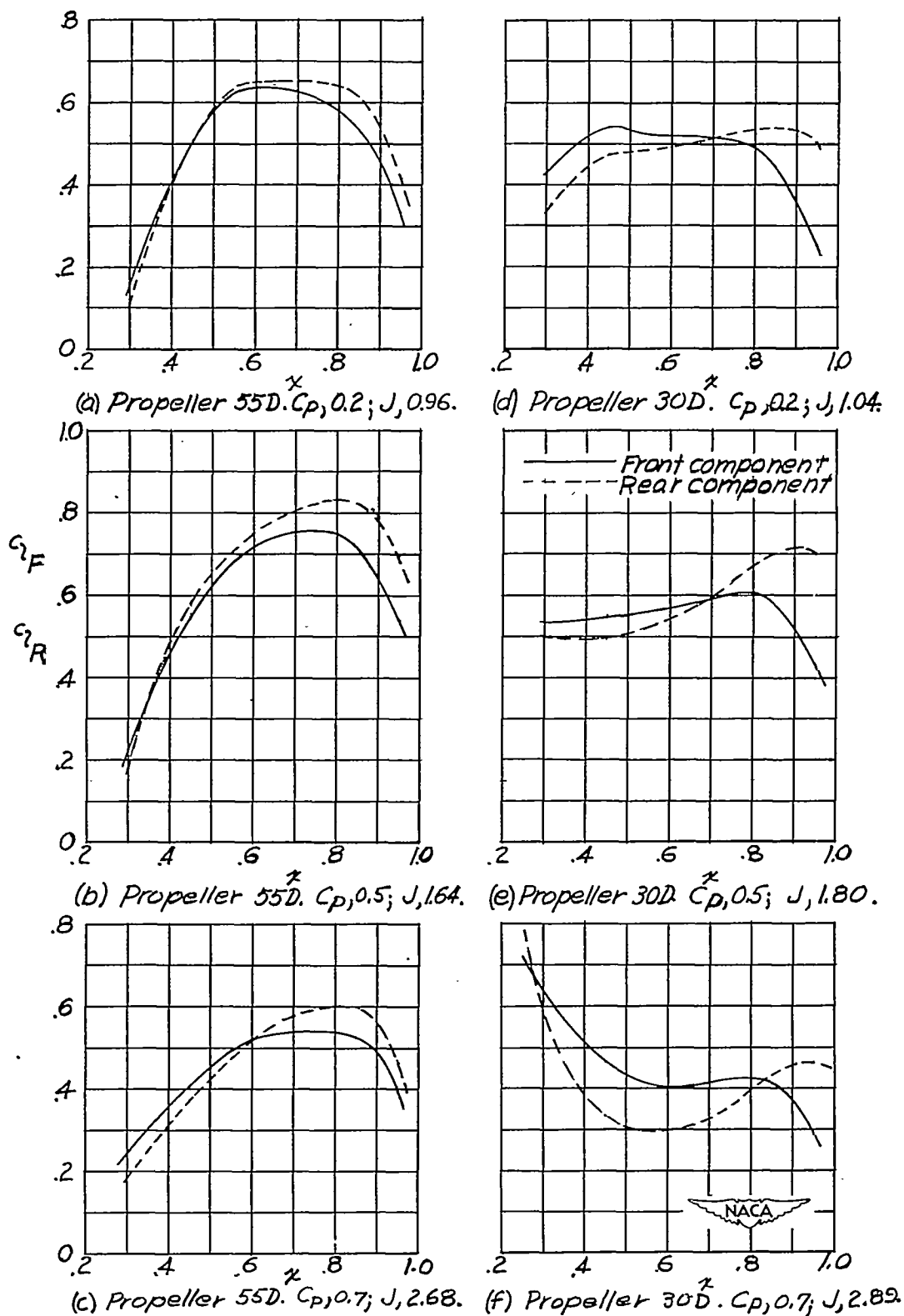


Figure 18. — Distribution of  $c_l$  for various flight conditions.

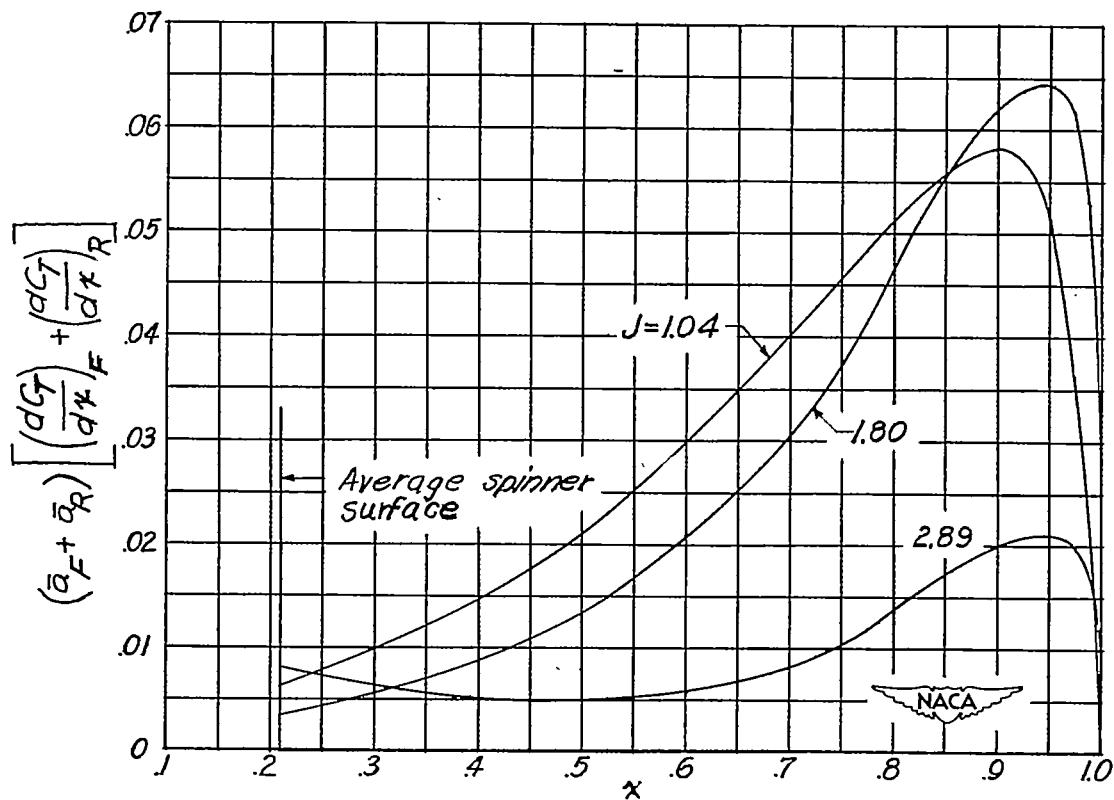


Figure 19.- Distribution of axial-momentum-loss factor, Propeller 30D.

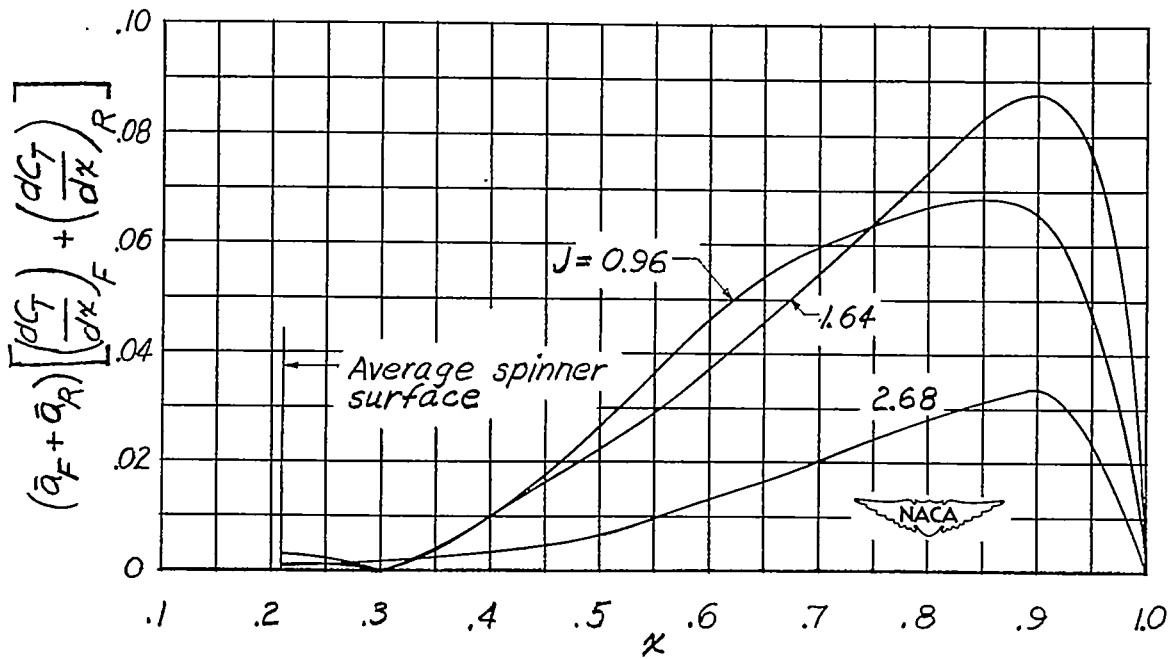


Figure 20.- Distribution of axial-momentum-loss factor, Propeller 55D.

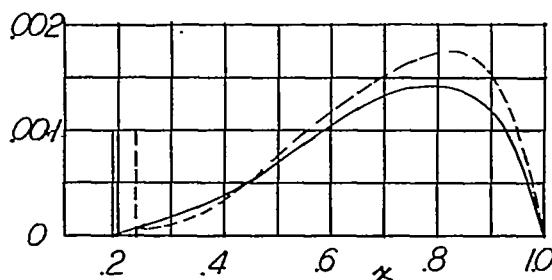
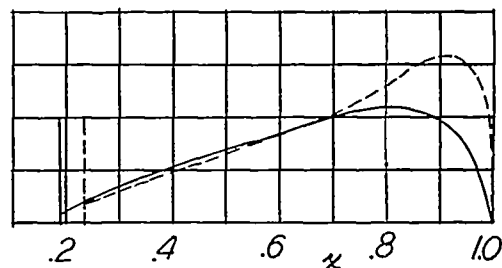
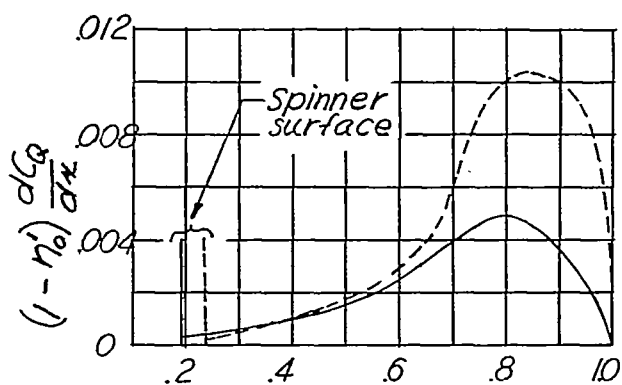
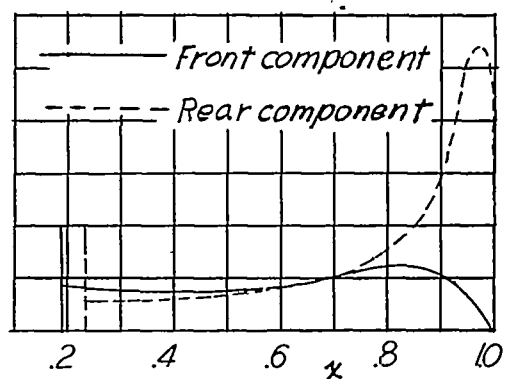
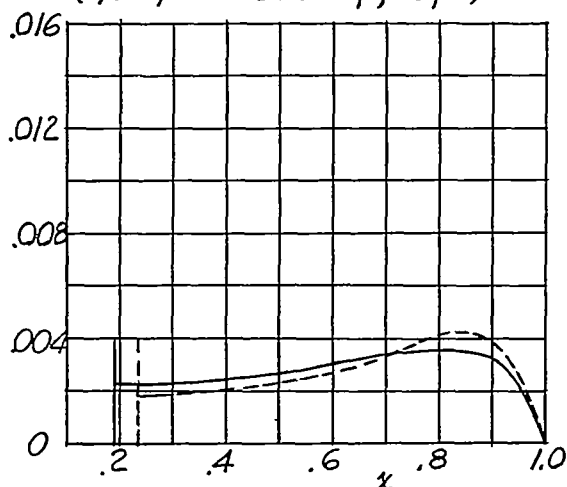
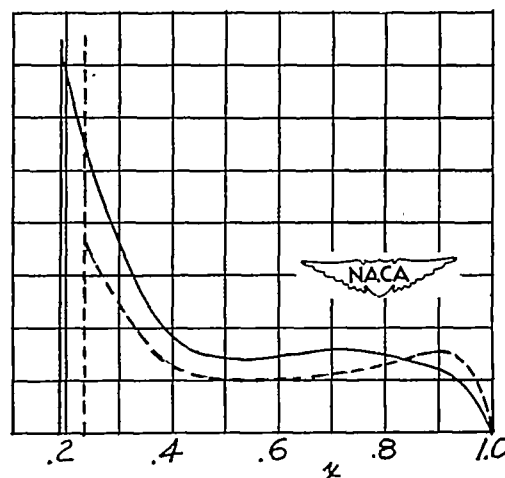
(a) Propeller 55D.  $C_p, 0.2$ ;  $J, 0.96$ .(d) Propeller 30D.  $C_p, 0.2$ ;  $J, 1.04$ .(b) Propeller 55D.  $C_p, 0.5$ ;  $J, 1.64$ .(e) Propeller 30D.  $C_p, 0.5$ ;  $J, 1.80$ .(c) Propeller 55D.  $C_p, 0.7$ ;  $J, 2.68$ .(f) Propeller 30D.  $C_p, 0.7$ ;  $J, 2.89$ .

Figure 21.—Distribution of profile-drag energy losses.